Publications of the Astronomical Society of Japan, 2024, **00**, 1–19
doi: 10.1093/pasj/xxx000
Advance access publication date:

Molecular star formation law in the Galactic Center by ACES (ALMA central molecular zone exploration survey)

Yoshiaki SOFUE,[1] Steven N. LONGMORE,[2,3] Daniel WALKER,[4] Adam GINSBURG,[5] Jonathan D. HENSHAW,[2,6] John BALLY,[7] Ashley T. BARNES,[8] Cara BATTERSBY,[9] Laura COLZI,[10] Jennifer WALLACE,[9] Jairo ARMIJOS-ABENDAÑO,[11] Nazar BUDAIEV,[5] Rojita BUDDHACHARYA,[2, 12] Rei ENOKIYA,[13] Christoph Federrath,[14] Zi-Xuan FENG, [15,16] Pablo GARCÍA,[17,18] Simon C. O. Glover,[16] Katarzyna M. DUTKOWSKA,[18,19], Savannah GRAMZE,[5] Christian HENKEL,[19] Pei-Ying HSIEH,[13] Yue HU,[20] Ralf S. KLESSEN,[16,21] Janik KAROLY,[22] Kotaro KOHNO,[1] Dani LIPMAN,[9] Dariusz C. Lis,[23] Xing LU,[29] Mark R. MORRIS,[24] Francisco NOGUERAS-LARA,[25] Jürgen OTT,[26] Denise RIQUELME-VÁSQUEZ,[27] Víctor M. RIVILLA,[10] Howard A. SMITH,[12] Tsutomu TAKAMIYA,[1] Q. Daniel WANG,[28] and Qizhou Zhang[12]

[1]Institute of Astronomy, The University of Tokyo, Mitaka, Tokyo 181-0015, Japan
[2]Astrophysics Research Institute, Liverpool John Moores University, IC2, Liverpool Science Park, 146 Brownlow Hill, Liverpool L3 5RF, UK
[3]CCosmic Origins Of Life (COOL) , https://coolresearch.io
[4]UK ALMA Regional Centre Node, Jodrell Bank Centre for Astrophysics, Oxford Road, The University of Manchester, Manchester M13 9PL, United Kingdom
[5]Department of Astronomy, University of Florida, P.O. Box 112055, Gainesville, FL 32611, USA
[6]Max Planck Institute for Astronomy, Königstuhl 17, D-69117 Heidelberg, Germany
[7]Center for Astrophysics and Space Astronomy; Department of Astrophysical and Planetary Sciences; University of Colorado, Boulder, CO 80389, USA
[8]European Southern Observatory (ESO), Karl-Schwarzschild-Strasse 2, D-85748 Garching, Germany
[9]Department of Physics, University of Connecticut, 196A Auditorium Road, Unit 3046, Storrs, CT 06269, USA
[10]Centro de Astrobiología (CAB), CSIC-INTA, Carretera de Ajalvir km 4, Torrejón de Ardoz, 28850 Madrid, Spain
[11]Observatorio Astronómico de Quito, Observatorio Nacional, Escuela Politécnica Nacional, Interior del Parque La Alameda, 170136, Quito, Ecuador
[12]Center for Astrophysics | Harvard & Smithsonian, 60 Garden Street, Cambridge, MA, 02138, USA
[13]National Astronomical Observatory of Japan, 2-21-1 Osawa, Mitaka, Tokyo 181-8588, Japan
[14]Research School of Astronomy and Astrophysics, Australian National University, Canberra, ACT2611, Australia
[15]Como Lake centre for AstroPhysics (CLAP), DiSAT, Università dell'Insubria, via Valleggio 11, 22100 Como, Italy
[16]Universität Heidelberg, Zentrum für Astronomie, Institut für Theoretische Astrophysik, Albert-Ueberle-Str. 2, 69120 Heidelberg, Germany
[17]Chinese Academy of Sciences South America Center for Astronomy, National Astronomical Observatories, CAS, Beijing 100101, China
[18]Instituto de Astronomía, Universidad Católica del Norte, Av. Angamos 0610, Antofagasta, Chile
[18]Transdisciplinary Research Area (TRA) 'Matter' - Hertz Chair for Astrochemistry, Universität Bonn, Am Propsthof 49, 53121 Bonn, Germany
[19]Leiden Observatory, Leiden University, P.O. Box 9513, 2300 RA Leiden, The Netherlands
[19]MPIfR, Auf dem Hügel 69, Bonn, Germany
[20]Cahill Center for Astronomy and Astrophysics, California Institute of Technology, Pasadena, CA 91125, USA
[21]Universität Heidelberg, Interdisziplinäres Zentrum für Wissenschaftliches Rechnen, Im Neuenheimer Feld 225, 69120 Heidelberg, Germany
[22]Department of Physics and Astronomy, University College London, Gower Street, London WC1E 6BT, UK
[23]Jet Propulsion Laboratory, California Institute of Technology, 4800 Oak Grove Drive, Pasadena, CA 91109, USA
[29]Shanghai Astronomical Observatory, Chinese Academy of Sciences, 80 Nandan Road, Shanghai 200030, P. R. China
[24]Department of Physics and Astronomy, University of California, Los Angeles, CA 90095, USA
[25]Instituto de Astrofísica de Andalucía (CSIC), Glorieta de la Astronomía s/n, E-18008 Granada, Spain
[26]National Radio Astronomy Observatory, P.O. Box O, 1011 Lopezville Road, Socorro, NM 87801, USA
[27]Departamento de Astronomía, Universidad de La Serena, Raúl Bitrán 1305, La Serena, Chile

Received: , **Accepted:**
© 2024. Astronomical Society of Japan.

[28]Department of Astronomy, University of Massachusetts, Amherst, MA 01003, USA
*E-mail: sofue@ioa.s.u-tokyo.ac.jp

ORCID: 0000-0002-4268-6499, 0000-0001-6353-0170, 0000-0001-7330-8856, 0000-0001-6431-9633, 0000-0001-9656-7682, 0000-0001-8135-6612, 0000-0003-0410-4504, 0000-0002-6073-9320, 0000-0001-8064-6394, https://orcid.org/0009-0002-7459-4174, 0000-0003-3341-6144, 0000-0002-0533-8575, 0009-0004-0685-7678, 0000-0001-0000-0000, 0009-0004-0121-1560, 0009-0004-0121-1560, 0000-0002-8586-6721, 0000-0000-0000-0000, 0000-0003-0980-6871, 0000-0002-1313-429X, 0000-0002-7495-4005, 0000-0001-9155-3978, 0000-0002-8455-0805, 0000-0002-0560-3172, 0000-0001-5996-3600, 0000-0002-4052-2394, 0000-0002-5776-9473, 0000-0002-0500-4700, 0000-0003-2619-9305, 0000-0002-6753-2066, 0000-0002-6379-7593, 0000-0001-8224-1956, 0000-0001-5389-0535, 0000-0002-2887-5859, 0000-0000-0000-0000, 0000-0002-9279-4041, 0000-0003-2384-6589

Abstract

We investigate the Schmidt relation in the CMZ (central molecular zone) through intensity-to-intensity correlation analysis of the H40α recombination line, 93.7 GHz radio continuum, CS (2-1) line intensity, and the emission measure (EM), using data from the ALMA CMZ Exploration Survey (ACES). Showing that the continuum, recombination line intensity, and EM are linearly correlated, we use the continuum as a measure of the relation and plot it against the CS (2-1) line intensity to construct the Schmidt plot. We further construct an EM-based SFR (star formation rate) to surface gas density relation, which we call the ACES SF diagram, and compare it with the current Schmidt relations of galaxies. The ACES diagram is categorized into three regions or branches, each with different properties: (A) The on-going SF branch, which has a forward Schmidt relation of index 2 as $SFR \propto \Sigma_{\rm H_2}^{2.0}$, indicating that the higher the gas density, the higher the SFR. This index suggests that star formation in the CMZ is triggered by cloud collisions. (B) The inverse Schmidt branch, having a negative index, that is caused by the artifacts of self- and backlight continuum absorption, as well as by the erosion of molecular clouds due to expanding HII regions; and (C) The basic, non-SF molecular region that dominates the CMZ shares 98% of the molecular mass without HII regions.

Keywords: Galaxy : center — HII regions — ISM: lines and bands — radio continuum: ISM — radio lines: ISM — stars: formation

f

1 Introduction

The Schmidt relation (Kennicutt-Schmidt relation or molecular star formation law), the unique fundamental relation that quantifies star formation activity in interstellar space and galaxies (Schmidt 1959; Kennicutt & Evans 2012), is defined as

$$SFR = A\,\Sigma^{\alpha}. \quad (1)$$

Here, SFR ($M_\odot$ kpc^{-2} yr^{-1}) and Σ ($M_\odot$ pc $^{-2}$) are the star formation rate and the surface density of the molecular gas, respectively, and A and α are constants. Extensive efforts to derive this relation have been made over the decades, leading to a relatively mild index (or slope in log-log plots) of $\alpha \sim 1-1.5$ (Kennicutt 1998; Heyer et al. 2004; Komugi et al. 2005; Komugi et al. 2006; Fuchs et al. 2009; Onodera et al. 2010; Kennicutt & Evans 2012; Evans et al. 2014; Willis et al. 2015; Sofue & Nakanishi 2017; Sofue 2017; Bacchini et al. 2019; Kennicutt & De Los Reyes 2021; Spilker et al. 2021; Elia et al. 2022; Sofue 2024), while some galaxies show a steeper index of $\alpha \sim 2$ (Boissier et al. 2003). Also, distinct SFR indices of $\alpha \sim 1,\ \sim -1,\ \sim 1$ for H_2, HI, and H_2+HI, respectively, have been obtained in the Milky Way disk (Sofue & Nakanishi 2017). On the other hand, a recent high-resolution study of resolved spiral arms of galaxies has obtained a steeper index of $\alpha \sim 1.85$ (Calzetti et al. 2026).

The trigger for star formation (SF) in molecular clouds has been one of the fundamental interests in Galactic astrophysics (Shu et al. 1987; Morris 1993; Lada & Lada 2003). Two major scenarios have been proposed that postulate either a stochastic (self-regulated) mechanism in individual clouds due to gravitational instability or sequential compression by expanding shells of HII regions (Elmegreen & Lada 1977; Myers 2009; Barnes et al. 2019; Hacar et al. 2023; Pineda et al. 2023), which postulate $\alpha \sim 1-1.5$, or external triggering by collisions of molecular clouds (Habe & Ohta 1992; Morris 1993; Hasegawa et al. 1994; Kimura & Tosa 1996; Stone et al. 2013; Fukui et al. 2021), which predicts $\alpha \sim 2$. However, a large scatter of the plots by an order of magnitude has made it difficult to constrain the formation mechanism more precisely, which is partly attributed to interstellar turbulence (Krumholz et al. 2012; Federrath 2013).

The overall SF activity in the CMZ (central molecular zone) is reported to be relatively low (Sofue 2022; Henshaw et al. 2023). This may be attributed to the suppression of the gravitational contraction of clouds due to the strong tidal effect (Sofue et al. 2026a), turbulence, magnetic pressure, and/or disturbances from the activity of the nucleus. A turbulence-regulated SF mechanism has been applied to the Brick cloud, explaining its low SF activity (Federrath et al. 2016; Barnes et al. 2017).

The Schmidt law plays an essential role in studying these star formation mechanisms in the Galactic Center. However, a thorough determination of the star formation law in the GC has not been obtained, as the current studies are primarily based on optical recombination lines such as the Hα line (Kennicutt & Evans 2012), but optical observations are affected by the high opacity in the direction of the GC. To solve this problem, radio recombination lines (RRLs), continuum free-free emission (Bremsstrahlung), and molecular lines provide a means to efficiently and directly determine the necessary quantities, such as SFR and molecular gas mass.

In this paper, we investigate the Schmidt relation in the CMZ using data from ACES (ALMA CMZ Exploration Survey), which has greatly expanded the possibilities for investigating the detailed properties of the CMZ, not only in molecular lines but also in recombination lines and continuum emission (Longmore et al. 2026; Ginsburg et al. 2025; Walker et al. 2026; Lu et al. 2026; Hsieh et al. 2026; Battersby et al. 2026; Sofue et al. 2025; Sofue et al. 2025; Paré et al. 2026). We use the H40α line at 99.02295 GHz, the continuum data at 93.7 GHz with a bandwidth of 4.7 GHz, which traces the free-free emission from the HII regions, and CS ($J = 2-1$), hereafter CS (2-1) , line (97.98095 GHz) maps for the molecular gas. CS was chosen because it is the simplest molecule after CO and is most often used in the literature after CO. Other lines will be also important and interesting, so that we provide related plots in the Appendix. We adopt a distance of $R_0 = 8.178$ kpc to the Galactic Center (Gravity Collaboration et al. 2019).

2 Data

We use the publicly available data products of the ALMA Central Molecular Zone Exploration Survey (ACES; project code 2021.1.00172.L, PI: S. Longmore), a Cycle 8 ALMA Band 3 (85–102 GHz) Large Program that mapped the inner ~ 100 pc of the Galaxy over $l = 359^\circ.4$ to $0^\circ.8$ and $|b| \leq 0^\circ.25$ region (Longmore et al. 2026). The survey was observed as 45 contiguous sub-mosaics, combining the ALMA 12-m, 7-m, and Total Power arrays — at present, the largest mosaic produced by ALMA — reaching an angular resolution of $\sim 2''$, corresponding to ~ 0.1 pc at the adopted distance. The H40α radio recombination line and CS (2-1) line lies in one of the two broad upper-sideband spectral windows and are released as part of the broad-window line products (Hsieh et al. 2026), while the continuum data reduction is described in Ginsburg et al. (2025). We also use the HNCO (J=4–3) line at 87.925238 GHz representative of high-density clumps of 10^{5-6} H_2 cm^{-3} (Jackson et al. 1984), which is more transparent than the CS line against continuum. This line is contained in one of the lower relatively narrow sideband windows (58.59 MHz, roughly equivalent to 200 km s^{-1}) and has already been used in previous studies using ACES data (Nonhebel et al. 2024; Battersby et al. 2026; Paré et al. 2026; Walker et al. 2026).

For the recombination line analysis, we use the H40α peak-intensity and velocity-integrated (moment 0) maps, in units of Jy beam^{-1} and Jy beam^{-1} km s^{-1}, respectively. For the molecular line, we use the CS (2-1) and HNCO (4-3) line intensities. The FWHM synthesized beams for CS (2-1) , HNCO(4-3) and H40α lines were $\theta_{\rm Line} = 2''.45$, corresponding to a linear resolution of 0.097 pc. For the continuum, we use the ACES aggregate 3-mm image at a representative frequency of 93.7 GHz (effective bandwidth 4.7 GHz), restored to a circular beam of $\theta_{\rm Conti.} = 2''.45$ (Ginsburg et al. 2025).

The RMS noise, as measured in the quietest regions on the maps, is ~ 0.1 mJy beam^{-1} for the 93.7 GHz continuum, ~ 1 mJy beam^{-1} km s^{-1} for CS (2-1) integrated intensity map, ~ 10 mJy beam^{-1} for HNCO integrated intensity map, and ~ 7 mJy beam^{-1} for the H40α peak intensity map. All maps share a common grid of $0''.5$ pixels in Galactic coordinates (GLON–TAN, GLAT–TAN), centered near $(l, b) = (0^\circ.143,\ 0^\circ)$ and spanning the full ACES footprint.

3 TT plot (scatter-plot) method

We apply the TT plot (scatter plot) to the ACES CMZ maps at various line and continuum emissions to examine the correlation of the intensities of different species. Here, the TT (antenna/brightness temperature to antenna/brightness temperature) plot is a representation of pixel intensities of the same mapped area at different frequencies or emission species in the log-log diagram, originally introduced for the spectral analysis of radio continuum maps (Uyanıker et al. 2004).

3.1 Correlations between continuum intensity, emission measure, recombination and molecular line integrated intensities

Figure 1 shows the maps used for the analysis in this paper, which include the 93.7 GHz continuum, H40α integrated intensity, and CS (2-1) line intensities taken from the ACES database, along with the emission measure from our previous paper (Sofue et al. 2026b) and the 1.4 GHz MeerKAT image from Heywood et al. (2022), overlaid on the CS (2-1) line map. Figure 2 shows overlays of the H40α peak intensity and CS (2-1) integrated intensity maps of representative regions such as Sgr B2, Sgr B1, Sickle and Pistol, Bridge (thermal filaments), Sgr A, and Sgr C regions.

The HII regions are visible in the H40α integrated and peak intensities (RRL), emission measure EM, and 93.7 GHz continuum maps in red, while the CS (2-1) line map is plotted in green, showing emission distributed over the CMZ in clumps, clouds, and filaments. It is impressive that there is not a clear spatial correlation between the star-forming regions represented by the RRL and continuum emission and the gaseous distribution shown by the CS (2-1) line map in green, which is due to the very small fraction of star-forming molecular clouds, as shown in subsection 8.4.

An exception is the Sgr B2 region, where the H40α emission and EM-bright regions are embedded in complicated molecular clouds and filaments. Other regions, such as Sgr B1, Sickle, Pistol, and Bridge, are located in relatively less bright regions in the CS (2-1) line. The Minispiral is bright in RRL and continuum emission but is not clearly visible in the CS (2-1) line. On the contrary, 20- and 50-km s^{-1}molecular clouds are evident and bright, but no outstanding HII regions appear to be associated, insofar as the present maps are concerned.

3.2 93.7 GHz continuum as a good tracer of SF regions

The direct tracers of the SF regions are the emission measure (EM) and the recombination line. However, the line maps are ~ 100 times less sensitive than the continuum because the line spectral resolution (bandwidth ~ 0.0003 GHz) is much narrower than the continuum bandwidth (4.7 GHz), despite the intensities (antenna temperatures) of H40α and the continuum being comparable. We therefore employ the continuum map to trace the HII regions by confirming that the 93.7 GHz continuum intensity is linearly correlated with H40α intensity and EM.

Figure 3 shows TT plots of various emissions of the CMZ, where a TT (scatter) plot is a representation of intensities in two different maps. This method was originally used to derive the spectral index using two maps of antenna temperatures $T_{\rm A}$ at two different wavelengths, both having different baseline levels.

The small dots represent intensities at individual pixels; there are a total of $NAXIS1 \times NAXIS2 = 11120 \times 4080 \sim 4.5 \times 10^7$ pixel points for the entire map, with each pixel size measuring $0''.5 \times 0''.5$ on the sky, including blanks. Therefore, the total number of data points is $N \sim 2 \times 10^7$ for the entire CMZ, or less, proportional to the area of the region analyzed. The black dots are the means of y (vertical)-axis values in linear scaling averaged in the log x bins at interval of 0.05 dex. The error bars are the standard errors (SE) defined by the standard deviation (SD) divided by the square root of the independent number of observations, $SE = SD/\sqrt{N/n}$, where N is the total pixel number in each bin and $n = (\mathrm{FWHM/pixel\ size})^2 = (2''.45/0''.5)^2)$ is the number of redundant pixels in the telescope beam.

The plots show that the continuum intensity, H40α line integrated intensity, and emission measure are linearly correlated with each other, as indicated by the straight lines inserted in the figures. The Pearson's r coefficient for EM to $I_{93.7\rm GHz}$ and log EM to log $I_{93.7\ \rm GHz}$ plots is calculated to be $r_{\rm Pearson} = 0.9526$ and 0.9496, respectively. This linear correlation indicates that the continuum emission at 93.7 GHz is a good tracer of HII regions and, hence, the star formation rate in the CMZ, complementing the RRL and EM maps with higher sensitivity, as shown above. From the plot,

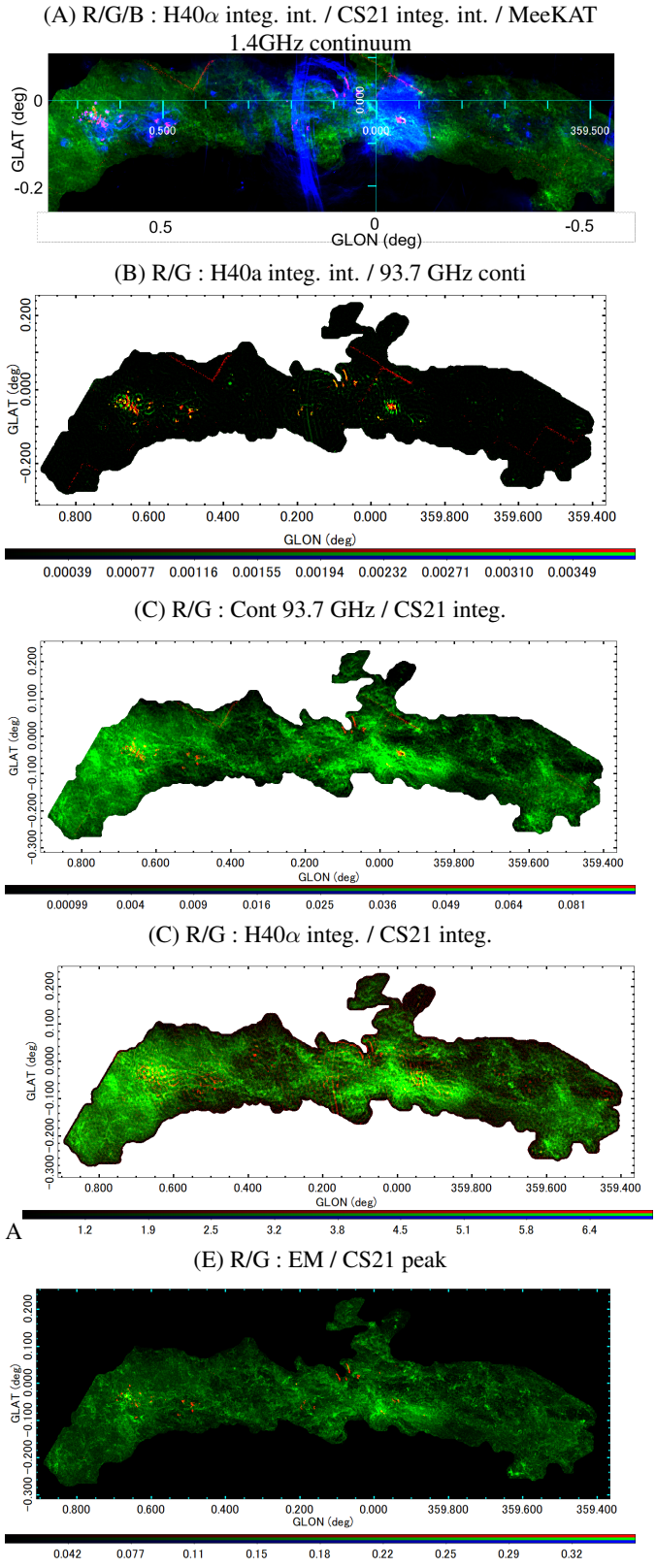


Fig. 1. [A] RGB overlay of H40α integrated intensity (red), CS (2-1) integrated intensity (green) and 1.4 GHz MeerKat continuum intensity (blue) (Heywood et al. 2022) maps of the CMZ . [B] 93.7 GHz continuum overlaid on H40α integrated intensity, showing good correlation, implying that the 93.7 GHz continuum is mostly thermal. [C] H40α integ.int. (red) overlaid on CS (2-1) integ. (green) showing distinct distributions. [D] EM map (red) (**?**) on CS (2-1) integ. (green). Alt text: Overlays of continuum, H40α, EM maps on CS (2-1) integ. intensity map.

we find that the emission measure is approximately expressed by

$$\frac{EM}{(\mathrm{pc\ cm^{-6}})} \simeq 1.0 \times 10^8 \frac{I_{93.7\mathrm{GHz}}}{(\mathrm{Jy\ beam^{-1}})} \quad (2)$$

Based on this linear relation, we hereafter employ the 93.7 GHz continuum map as the tracer map of SFR.

4 Schmidt relations

4.1 ACES diagram for star formation relation

We define a "Schmidt plot" as a TT plot of 93.7 GHz continuum, RRL (H40α integrated intensity), or EM on the vertical axis as a representative of SFR, plotted against CS (2-1) line integrated intensity on the horizontal axis as a representative of the surface density of dense gas. This plot will be later named the "ACES SF diagram".

According to the empirical relation given by equation (2), we hereafter employ the 93.7 GHz intensity as the representative of SFR in place of EM and H40α intensity because the continuum emission is the most sensitive among the three.

Figure 4 shows Schmidt plots for the entire CMZ in the region enclosed by the largest square in Figure 5. The H40α, 93.7 GHz continuum intensity, and EM plots show almost the same dependence against CS (2-1) integrated intensity as a trivial result of the linear relations found in Figure 3. The black dots with error bars are the running means of the vertical values in linear scale, averaged in bins along the horizontal axis, taken every 0.1 dex increment with the same width. The errors are the standard errors of the mean values in each bin.

A notable characteristic observed in the plot is the bimodal bifurcation of the data point distribution, extending from the densest region (centered around the lowest intensity in the 93.7 GHz band, $I_{94\mathrm{GHz}} \sim 1$ mJy beam^{-1}, and the average CS intensity across the entire map, $I_{\mathrm{CS}} \sim 5$ Jy beam^{-1} km s^{-1}) toward the upper right and upper left of the panel. This is more clearly seen by plotting the running means of the data points (black dots with error bars), which show that the continuum intensity (SFR) increases toward the upper right and upper left from the densest center of the plot.

Most interestingly, the right side branch extends straight in the log-log plot, as observed more clearly in the enlarged plot in the bottom-right panel of the figure. The plot is well fitted by a line expressed by

$$EM \simeq 1.0 \times 10^5 I^2_{\mathrm{CS.integ.int.}}, \quad (3)$$

indicating a steep Schmidt index of $\alpha = 2$. So, we summarize that the right half of the Schmidt plot indicates a 'forward-Schmidt' law with index +2, or $SFR \propto \Sigma^2_{\mathrm{gas}}$.

On the contrary, the left side branch shows an inverse proportionality to the gas density. This branch is due to absorption of the CS line against strong backlight HII emission and/or due to erosion of the cloud by HII expansion. The former is a kind of artifact, and does not appear in a plot using a more transparent line, HNCO (J=2–1), as will be discussed in the later section. .

For convenience, we name the three regions in the TT plot as (A) the forward Schmidt branch representing on-going star formation, (B) the reverse (inverse) Schmidt branch as a mixture of artifact absorption of backlight HII emission and erosion of molecular clouds by HII expansion, and (C) the basic clouds as pre-SF regions, as indicated by the dashed areas in figure 4.

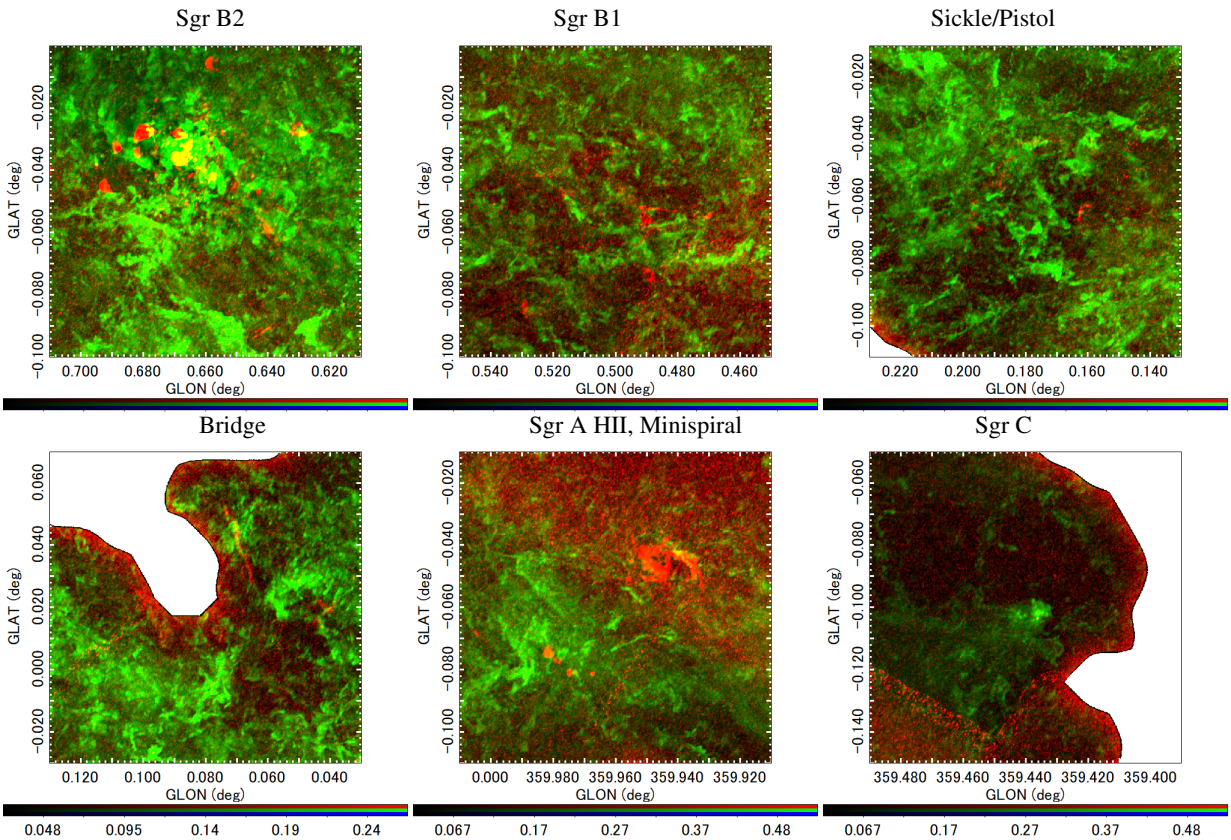


Fig. 2. RG overlay maps of H40α-line peak intensity (red) and CS (2-1) integrated intensity (green) Alt text: Overlay maps.

4.2 Individual regions

Figure 5 shows Schmidt plots for the individual regions enclosed by the squares marked in the intensity map in the top-left panel, along with the region names. Below, we describe the individual regions.

Sgr B3 : This off-plane extension of the molecular outskirts of the Sgr B2 complex is quite calm in star formation without a forward Schmidt branch. However, a post SF branch extends at a steep negative slope. The hyper-supernova explosion that drives the large molecular ring M+0.8-0.2 in this region (Nonhebel et al. 2024) may be a phenomenon related to the past SF activity that produced this inverse Schmidt branch.

Sgr B2 : The Schmidt plot for Sgr B2 is enlarged on the left-panel of figure 6. The Sgr B2 plot is remarkably similar to that of the entire CMZ (figure 4). This means that almost all the data points in region (A) are attributable to Sgr B2. Sgr B2 is exceptionally strong, while the other regions have much weaker intensity distributions; even adding them all together does not significantly alter the Schmidt plot for the CMZ. This indicates that most of the star formation activity at the Galactic Center is concentrated in the Sgr B2 region. For example, the result for Sgr C is overlaid and enlarged in the right panel for comparison, showing that the continuum emission is two orders of magnitude weaker than that in Sgr B2.

It is also pointed out that the inverse and forward Schmidt relations are more clearly observed in this plot, indicating that the plot for Sgr B2 is a mixture of two types of Schmidt relations: The forward Schmidt branch with a positive slope represents an on-going SF region in the densest molecular cloud. The inverse Schmidt branch with a negative slope is an artifact due to either the absorption of backlight HII continuum emission by the foreground cloud or erosion of molecular cloud bu HII expansion.

Sgr B1: The Schmidt branch is missing, possibly implying that Sgr B1 is a 'post-SF' site.

Quiet regions E and W: In these regions, there appear to be no particular H40α regions. Accordingly, the Schmidt plots are very calm, with low molecular column densities.

Brick: This cloud lacks the Schmidt branch; hence, the SF is not so strong..

Sickle/Pistol : A weak forward-Schmidt nature is observed, suggesting that these are on-SF regions, but overall SF does not seem very strong.

Bridge (thermal filaments): This is composed of extended HII regions, with no signs of active SF.

50-km s^{-1}cloud and Sgr A HII regions: HII regions are relatively bright, and the gas density is high, but no Schmidt alignment is recognized.

CND and Minispiral: This is the central part of the CMZ and shows a similar Schmidt relation to that of Sgr B2. However, the forward branch is much shorter and weaker, indicating that the cloud collision mechanism does not apply here. On the other hand, the inverse-Schmidt branch is prominent, with HII regions destroying the surrounding clouds.

20-km s^{-1}cloud: This is a high density molecular region without clear Schmidt branch.

Sgr C: The Schmidt plot is shown in figure 6 in comparison with Sgr B2 and is enlarged in the bottom panel. The vertical scale is 1/100 of that of the other panels. In Sgr C, the forward Schmidt branch is prominent, indicating that on-going star formation dom-

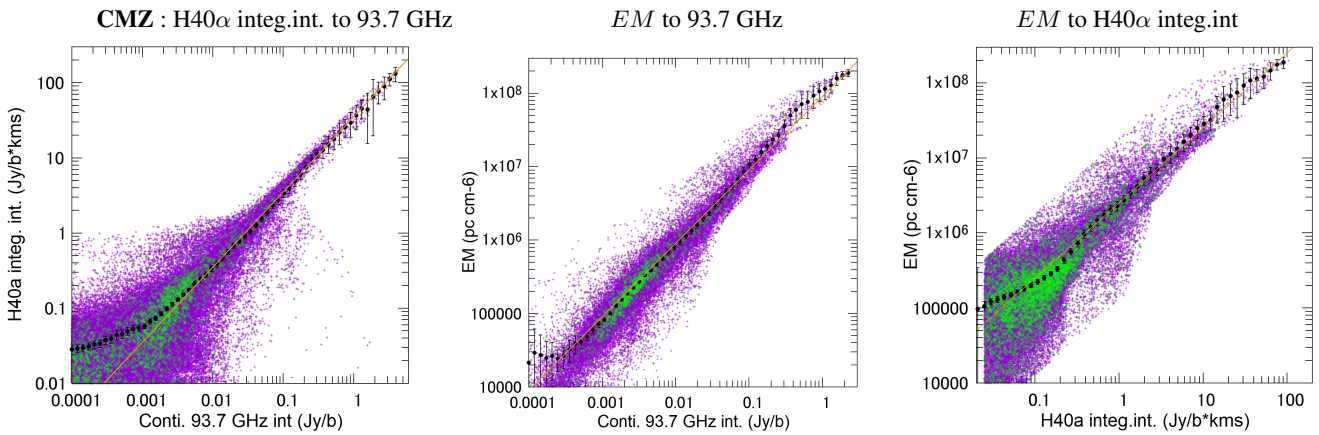


Fig. 3. TT plots (scatter plots) among the H40α (RRL) integrated intensity, emission measure EM, and 93.7 GHz continuum in the CMZ, showing a linear correlation as traced by the straight lines. Pearson's r coefficient for EM to 93.7 GHz plot (center panel) is as high as $r = 0.95$ both in log-log and linear-linear space, indicating that the continuum intensity is a good indicator of the star formation rate represented by the RRL and EM. Saturated regions are highlighted by green dots, every 100 of the violet (original) points. Alt text: TT plots

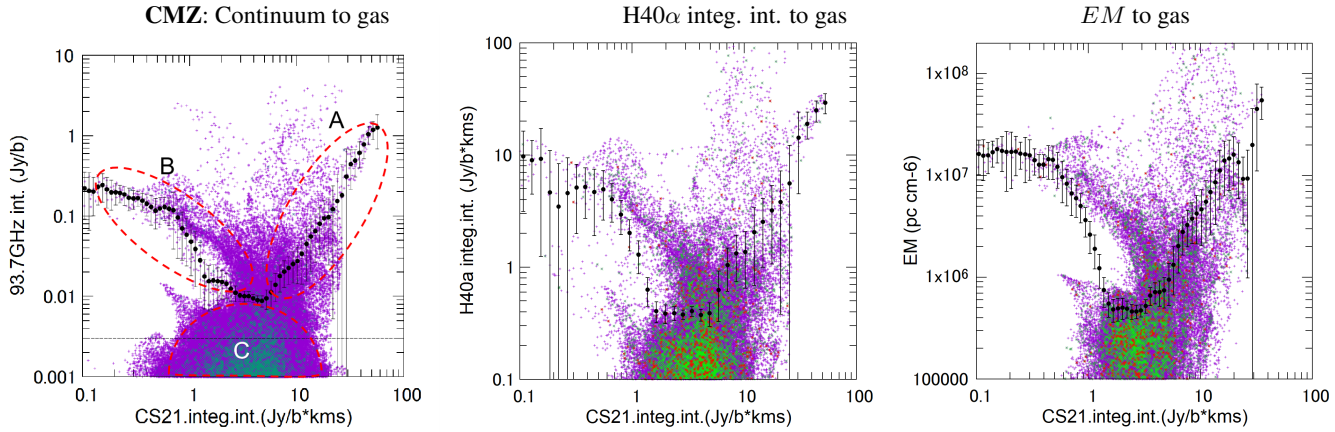


Fig. 4. "TT-Schmidt plot", or "ACES SF diagram": The 93.7 GHz continuum intensity, H40α line integrated intensity, and EM plotted against CS (2-1) -line integrated intensity in the CMZ, showing the forward and inverse (reverse) Schmidt relations. For later convenience we divide the plot into three regions named (A) the forward Schmidt branch as for on-going SF regions, (B) reverse (inverse) Schmidt branch as due to absorption of backlight HII emission, and (C) basic (background) cloud region as for pre-SF molecular gas with weak or no associated HII emission. Large dots with error bars show running means of the plots. The horizontal dashed line in the left panel indicates the lower limit of running averaged means in order to avoid regions (C). Saturated regions are highlighted by green dots, every 100 of the violet points. Alt text: Schmidt and inverse Schmidt relation.

inates.

4.3 Schmidt plots of the central parsecs of Sgr B2, B1 and Sgr C

In the previous sections, we dealt with the average values of individual regions of 20–30 pc in size. As a result, the properties of individual HII regions were smoothed out, and the individuality of each region has weakened. In this subsection, we create and compare Schmidt plots limited to 2 pc $\times$ 2 pc squared areas for Sgr B2 North, Main, and South, Sgr B1, and Sgr C.

Figure 7 displays these plots on the same scale. The bimodal property of the Schmidt relation is more evident in this figure. The straight line is a fit to the forward Schmidt relation with $\alpha = 2$ for reference, approximately fitted to Sgr B2 North. A similar forward relation with about the same slope of $\alpha \sim 2$ is observed in B2 Main, B2 South, and Sgr C, while the vertical intensities vary by an order of magnitude, with B2 Main being the highest.

Sgr B1 lacks the forward Schmidt branch not only in the central 4 pc $\times$ 4 pc area but also in the larger area of $\sim$ 20 pc $\times$ 20 pc square, as shown in figures 5 and 7. Therefore, Sgr B1 is a unique SF region where there is no on-going star formation; maybe, the whole Sgr B1 is a post-SF region.

5 Schmidt relation in the position-velocity diagrams (PVD)

We have so far dealt with the Schmidt relation using the radio continuum emission and integrated molecular line intensity maps projected onto the sky. However, since the CMZ is a flattened disk viewed edge on, star-forming regions and molecular clouds along the line of sight are spatially overlapping, and the Schmidt relation is also smoothed. Therefore, in this section, we investigate the Schmidt relation using the line emissions alone, considering three-dimensional information that takes into account the extension in the velocity direction on the position-velocity diagrams.

The top panel of figure 8 shows position-velocity (PVD) or

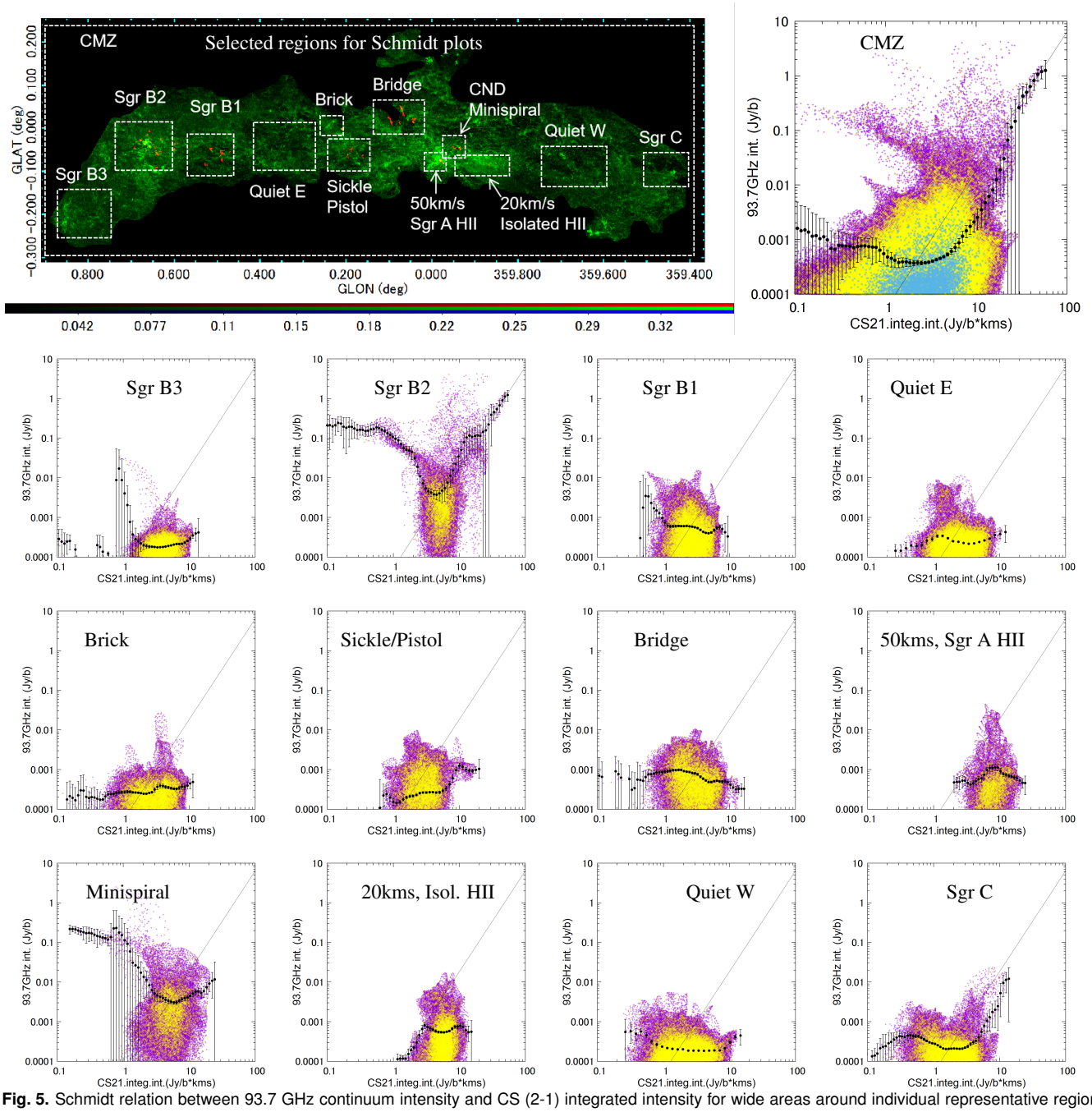


Fig. 5. Schmidt relation between 93.7 GHz continuum intensity and CS (2-1) integrated intensity for wide areas around individual representative regions shown in the top-left panel. The black dots are running means using all points in each horizontal bin and standard error in linear vertical scaling (Note that the mean was taken above the threshold to avoid region (C) .) Saturated density areas are re-plotted by yellow dots every 10 data points and blue every 1000 of the violet points. Alt text: Schmidt plots around representative regions

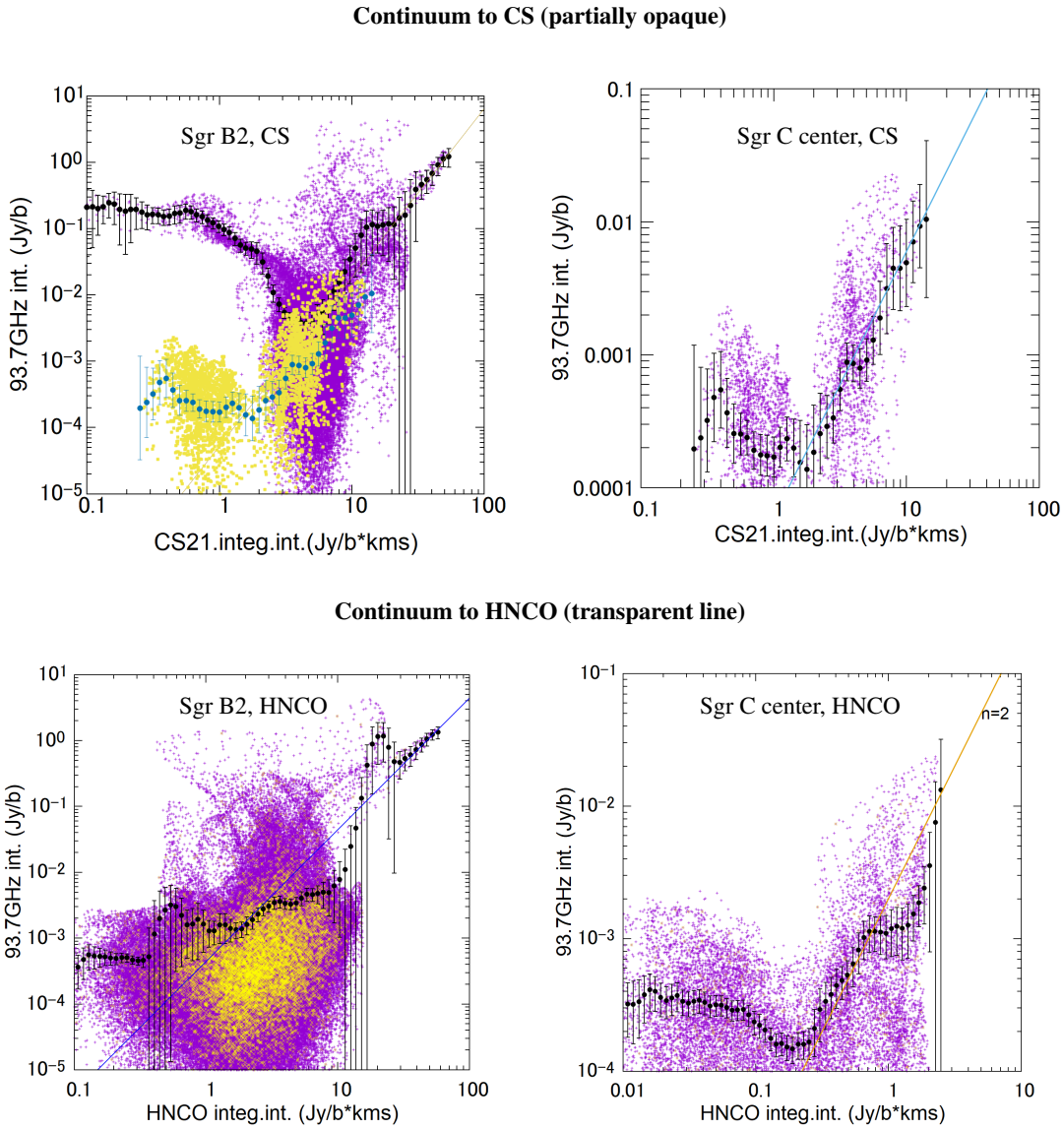


Fig. 6. [Top panels] Schmidt plots (ACES SF diagram) in the CS (2-1) line for Sgr B2 (left) and Sgr C (right), which is partially opaque and appear as absorption against strong continuum backlight of HII regions. The left plot for Sgr B2 is overlaid by Sgr C. [Bottom panels] Same, but in the HNCO line, which is transparent for the continuum emission. In all the panels, the forward branch shows up and aligns on about the same relation with $\alpha \sim 2$ as indicated by the straight lines. However, the reverse branch appears only in the CS-continuum plot for Sgr B2, which is an artifact due to absorption of strong backlight-HII continuum emission, while it does not appear in the other panels. Alt text: Forward and reverse Schmidt relations.

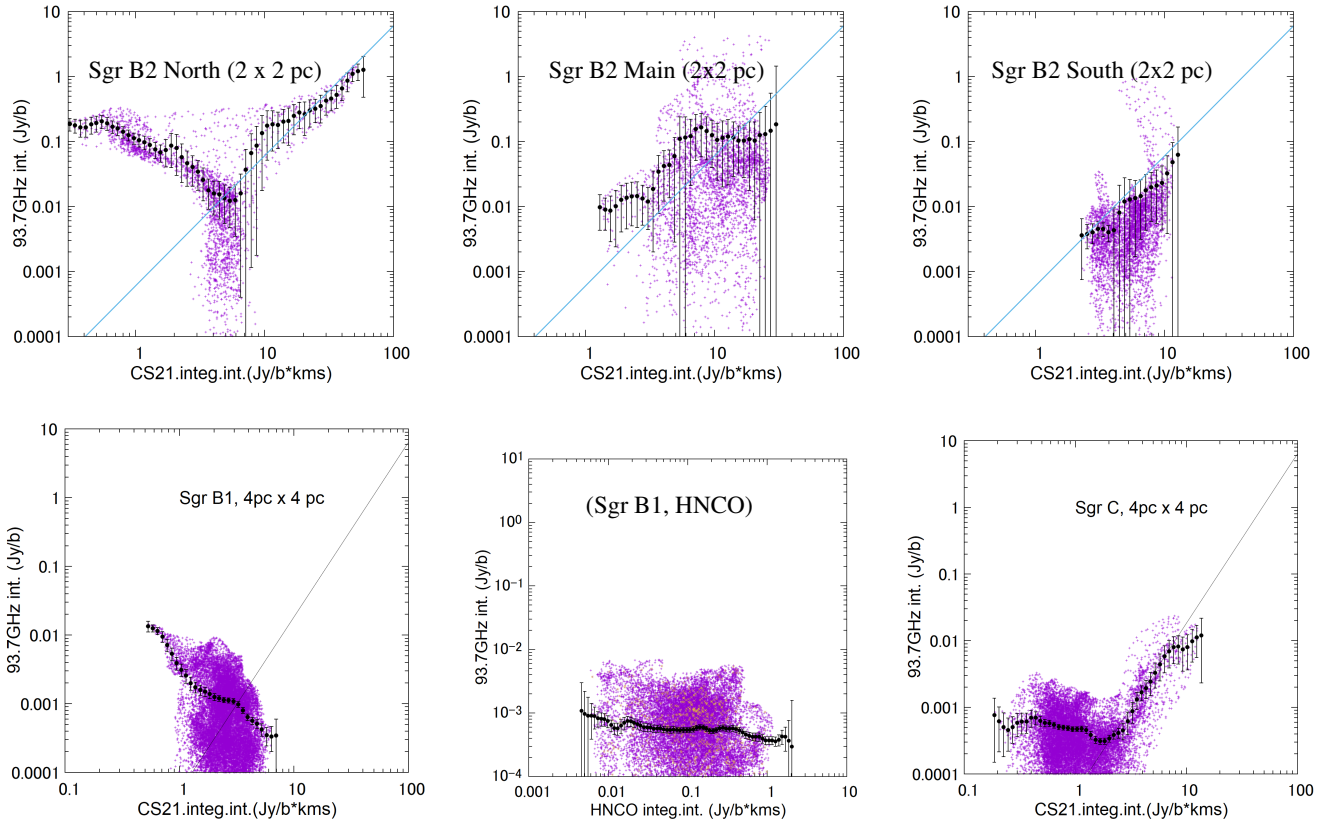


Fig. 7. Schmidt plots in $2\ \mathrm{pc}\ \times 2\ \mathrm{pc}$ regions centered on Sgr B2 N, B2 M and B2S, and $4\ \mathrm{pc}\ \times 4\ \mathrm{pc}$ on Sgr B1 and Sgr C in CS lines except for the bottom-middle small panel in the transparent HNCO line for Sgr B1. Straight lines indicate a power-law relation with $\alpha = 2$. Alt text: Schmidt relations.

longitude-velocity diagrams (LVD) of the CMZ in the H40α line peak intensities. The second panel shows an overlay of the H40α LVD in red on the CS (2-1) LVD in green. The representative SF regions are indicated by their names, and squares represent the regions in which the Schmidt plots are obtained. The 2nd and bottom panels are enlargements with contours for H40α intensity in order to investigate the correlation between the recombination and molecular line structures.

Only in the Sgr B2 region is the correlation between the RRL and molecular line intensity distributions clearly recognized. However, the CS (2-1) line is significantly affected by the absorption against the continuum emission of Sgr B2. For this absorption, the H40α intensity peaks do not necessarily coincide with CS (2-1) line peaks. On the other hand, the correlation is not evident in the other regions.

Nevertheless, we have created the Schmidt plots and show the results in figure 9 for the individual squared regions indicated in figure 8. As expected, only Sgr B2 and the entire CMZ show a forward Schmidt relation, which is fitted with a slope index $\alpha \sim 2$, as indicated by the straight line. Figure 9 shows the running mean of the relation for the forward Schmidt branch, along with the line with $\alpha = 2$. On the other hand, the other regions do not exhibit clear relationships.

6 TT plots using different molecular lines

This section describes TT plots among different molecular lines, although it is not directly related to the Schmidt analysis. Therefore, one may skip this section if focusing on the main topic of this paper.

6.1 TT between continuum and molecular lines

We have so far used the CS (2-1) line to sample relatively extended clouds because of its higher intensity compared to the other lines. Here, we compare the Schmidt plot with those created using different lines to examine how the plot behaves depending on the molecular species. Figure 10 shows plots of 94 GHz continuum intensity against six different molecular line integrated intensities from ACES with the same array configuration as the CS (2-1) line.

Generally, the horizontal scatter decreases with the mean intensity of the plots, such that the CS (2-1) line shows the tightest distribution and the SO($J = 2 - 1$) line the broadest. The forward Schmidt branch is observed in all the panels with $\alpha \sim 2$ for CS, $H^{13}CN$, and SiO, whereas the HCO^+ line shows a shallower index with $\alpha \sim 1.5$. We also note that this line does not show the reverse Schmidt branch.

Figure 11 shows a comparison between different molecular lines.The plot of $H^{13}CO$ vs. CS (2–1) lines shows a linear correlation with $\alpha = 1$, indicating that both represent the same molecular gas. We also present TT plots between more molecular lines in figures 18 and 19 for reference, which will be used in a separate paper in preparation discussing the molecular line properties.

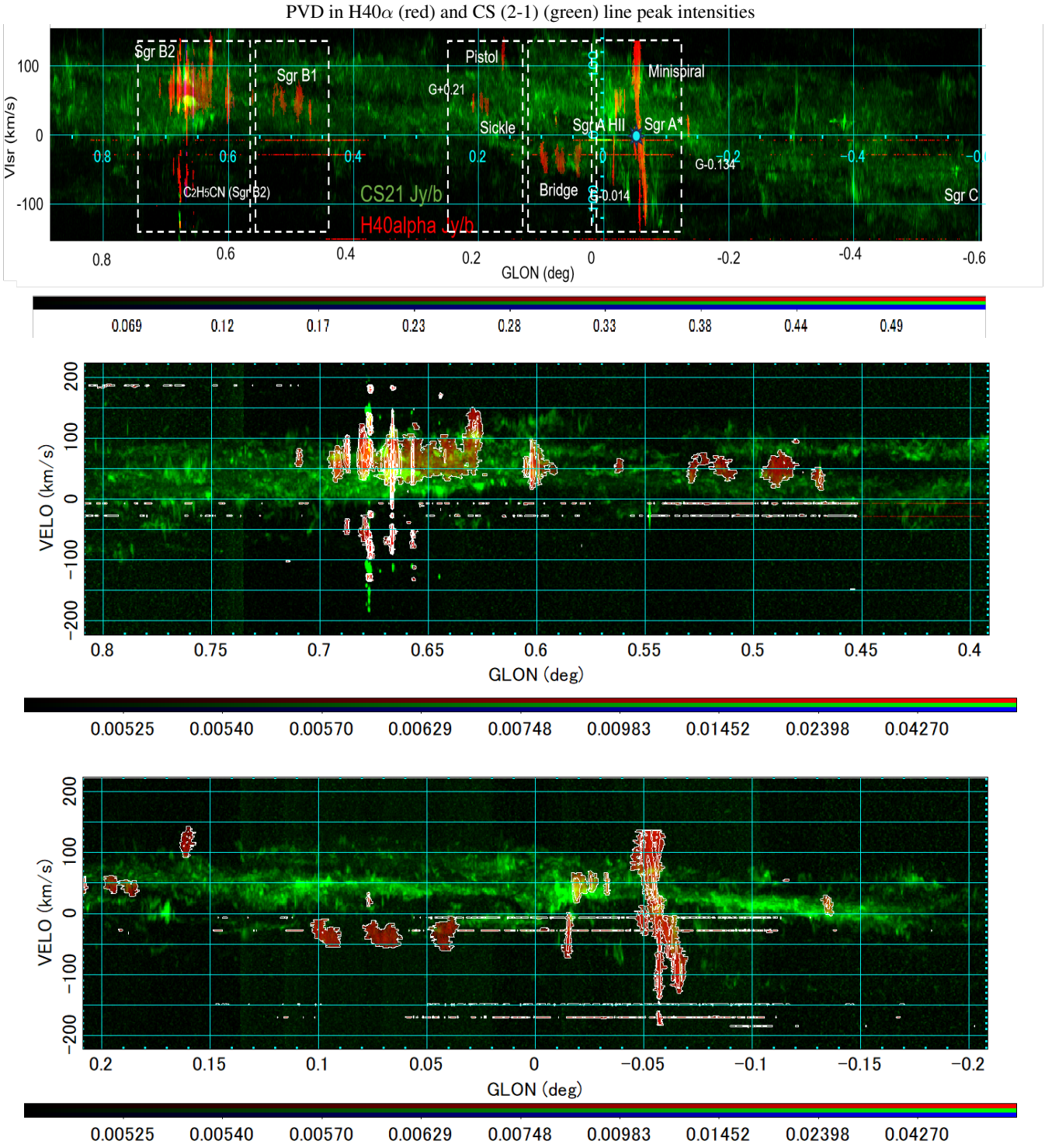


Fig. 8. [Top] Longitude-velocity diagram in the H40α in red and CS (2-1) lines in green. [Middle] Same, but enlarged around Sgr B1 and B2. [Bottom] Same, but around GC. Alt text: Continuum map and LVD in H40α and CS (2-1) line intensities.

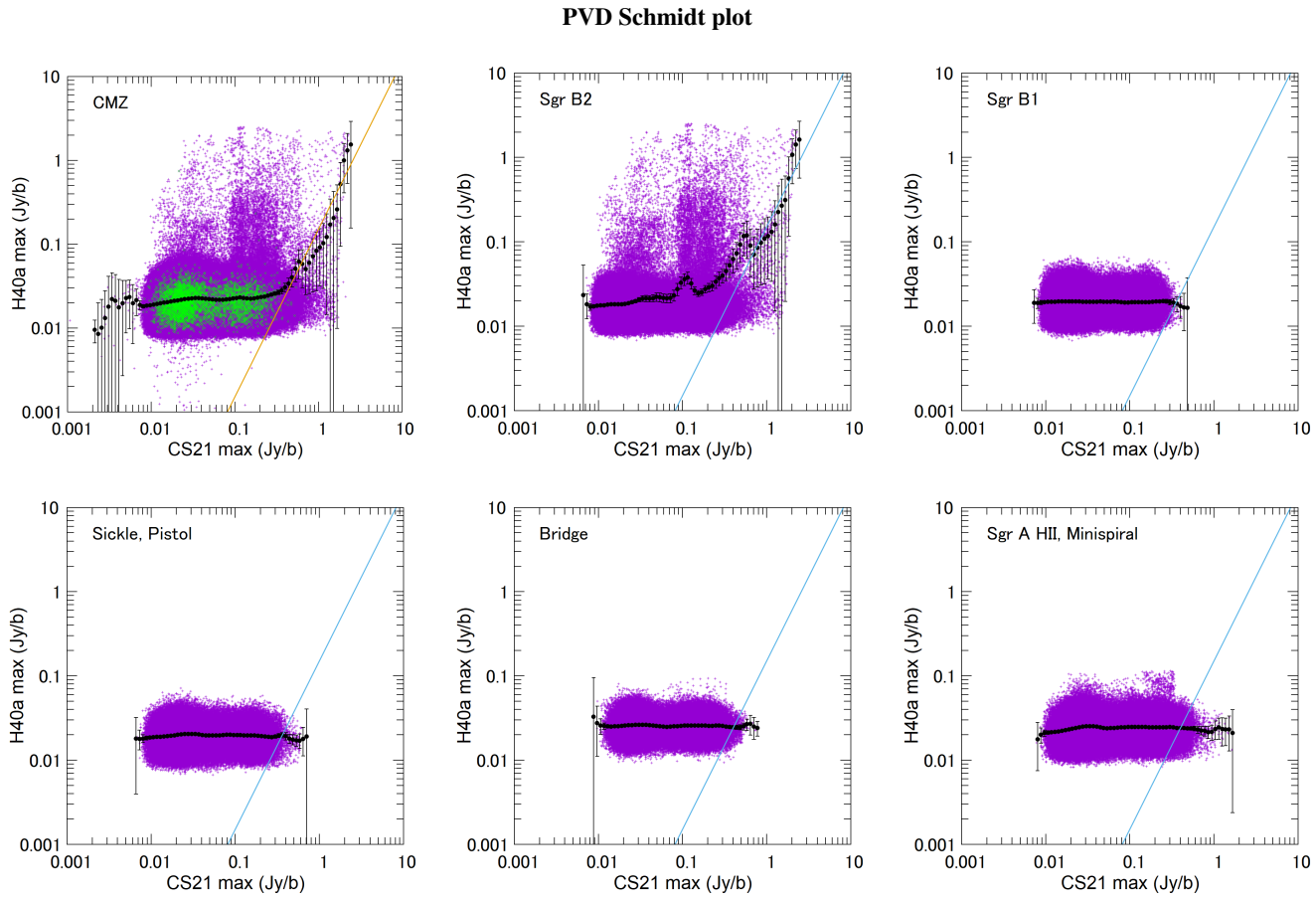


Fig. 9. Schmidt plot from PVDs. Alt text: Continuum map and LVD in H40α and CS (2-1) line intensities.

6.2 Photo-dissociation region (PDR)

The HCO^+ intensity plotted against CS (2–1) intensity does not show a linear correlation and instead resembles that of the continuum vs. CS (2–1) with $\alpha \sim 1.4$. This may indicate that HCO^+ behaves similarly to the continuum and H40α emissions, tracing ionized gas, as HCO^+ is considered a good tracer of PDR (photo-dissociation region). The HCO^+emission likely traces warm UV-illuminated surfaces of molecular clouds, while CS traces denser, colder, better-shielded regions, and H40α traces hotter and more extended ionized gas expanding outward. The shallower $\alpha \sim 1.4$ index may be explained if the HCO^+ line comes from the PDR of the surfaces of more compact and strongly bound molecular clouds due to self gravitation. HCO^+ usually has high opacities and can even be self-absorbed in the GC, so it could have an impact on its integrated intensity, making it more correlated to the molecular gas rather than to the HII region.

In figure 11 we compare the TT plots of $HCO^+$and H40α integrated intensities against CS (2-1) . In figure 12 we show TT plots for HCO^+ against CS (2-1) integrated intensity for the central region of Sgr B2, the Minispiral, and Sgr C.

The diagrams show that HCO^+intensity is about two orders of magnitude higher than H40α, suggesting that $HCO^+$and CS (2-1) may be a promising set for the SF analysis. However, $HCO^+$and H40α are not linearly correlated, as shown in the right panel of figure 11. Also, the HCO^+-to-CS (2-1) plots exhibit a shallower or more linear slope, as a natural consequence of the closer association of $HCO^+$with the molecular gas.

7 Star-formation relation

7.1 EM-based SF relation with $\alpha = 2$

We have obtained various TT plots between the emission measure, 93.7 GHz radio continuum emission, H40α peak and integrated intensities, and CS (2-1) integrated line intensity. The former four quantities are shown to be linearly correlated with each other, and any of them can be used to represent the star formation rate.

Since the 93.7 GHz continuum map is most sensitive to thermal emission regions, like HII regions, we used it to seek the general properties of the TT plot over the CMZ. However, it is less directly representative of the SFR than H40α and EM maps. The EM map represents the star formation rate almost directly, as it measures the exciting UV photon densities from the newly born OB stars while being less sensitive to the extended and fainter HII regions.

Therefore, with the sacrifice of detecting faint HII regions, we employ EM to construct an EM-CS (2-1) based Schmidt plot in order to obtain a more plausible star formation relation in the Galactic Center. Figure 13 shows the result, which exhibits a good power-law relation with $\alpha = 2.0$, as represented by the straight line resulting from least-squares fitting to the log-log plot using the increasing part of the plot at $I_{\rm CS21} \geq 3$ Jy beam^{-1}km s^{-1}and $I_{93.7GHz} \geq 0.001$ Jy beam^{-1}. The fitting was obtained using the equation,

$$\log \frac{EM}{(\mathrm{pc\ cm^{-6}})} = b + \alpha \log \frac{I_{\rm CS.integ.int.}}{(\mathrm{Jy\ beam^{-1}\ km\ s^{-1}})}, \quad (4)$$

we obtain $\alpha = 2.055 \pm 0.044$ and $b = 4.613 \pm 0.04$ (see also table

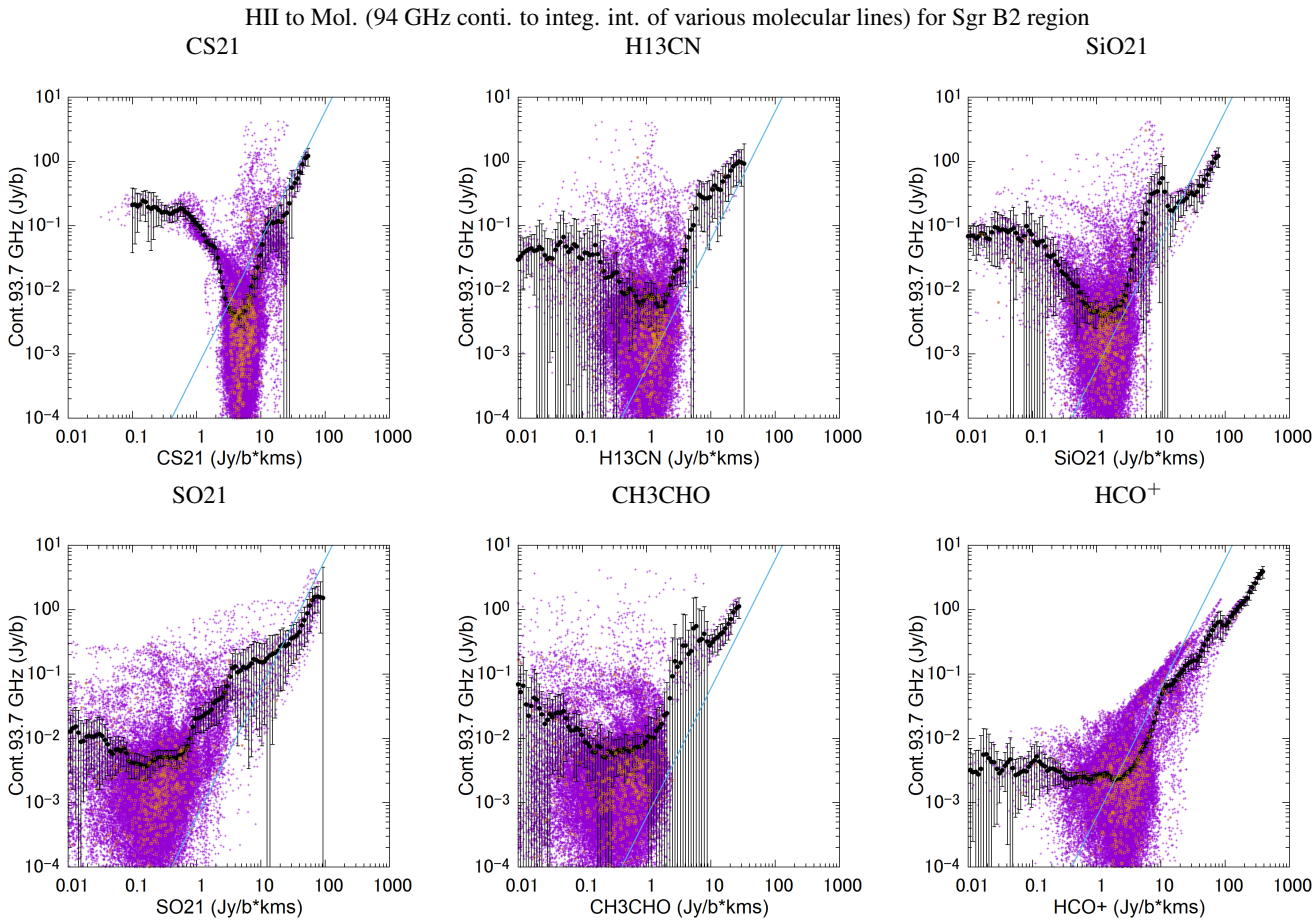


Fig. 10. Schmidt plots (ACES SF diagrams) between 93.7 GHz continuum and integrated intensity of six different molecular lines for the Sgr B2 region. The straight line indicates a power law with index 2 for reference. (TT plot matrix for full comparison is given in Appendix for further usage, which are not directly used in this paper.) Alt text: Schmidt plots by different molecular lines.

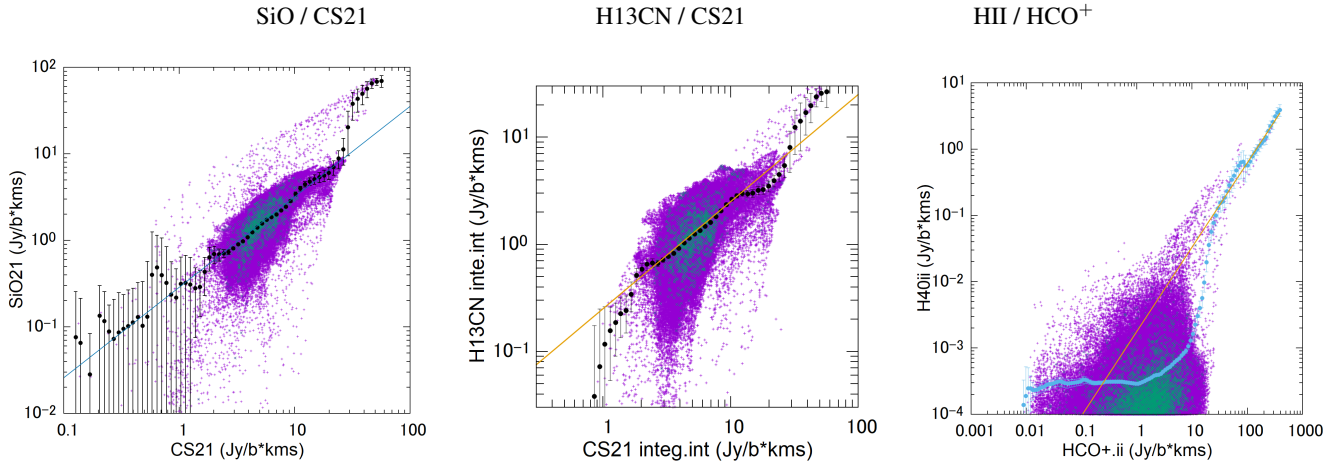


Fig. 11. Molecule to molecule plots for Sgr B2 region, showing an approximately linear regions: SiO to SO with $\alpha = 1.05$, H13CN to CS with $\alpha = 1$, and H40α to H13CN with $\alpha \sim 1.2$. (TT plot matrix for full comparison is given in Appendix.) Alt text: TT plots by different molecular lines.

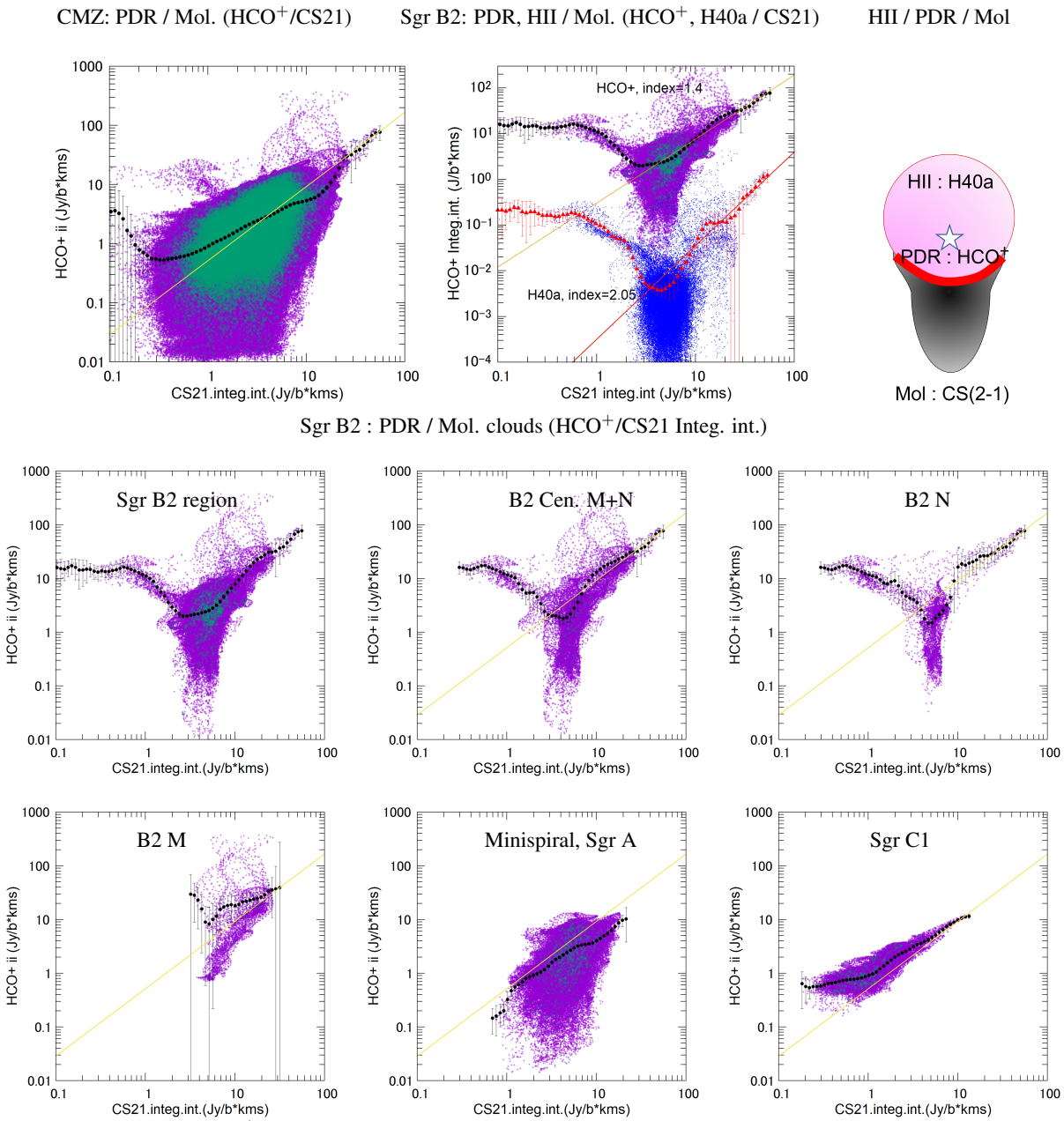


Fig. 12. [Top panels] TT plots for HCO$^+$(PDR) and H40α (HII region) lines in the Sgr B2 region against CS (2-1) integrated intensity. Fitted slopes are $\alpha = 1.4$ and 2.5, respectively. [Middle and bottom panels] TT plots of HCO+ vs CS21 in the central region of Sgr B2, Minispiral and Sgr C. Alt text: TT plot for PDR and HII regions. The straight lines indicates slope $\alpha = 1.4$

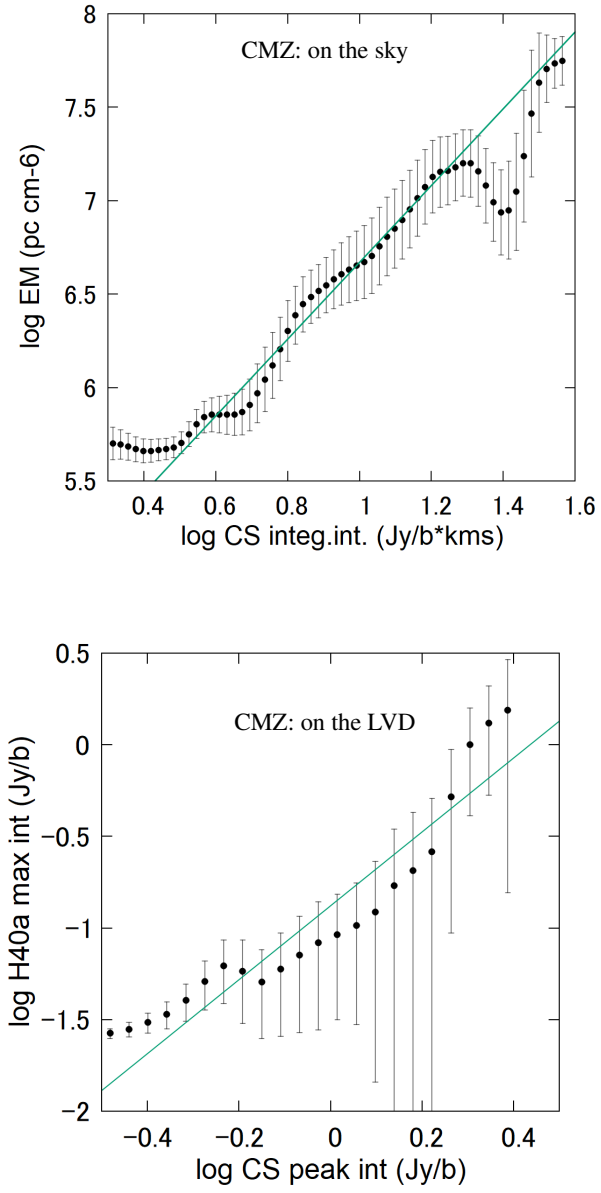


Fig. 13. Forward Schmidt in CMZ on the sky (top) and on the PVD (bottom). The lines are the least squares fit resulting in $\alpha = 2.055 \pm 0.044$, $b = 4.61342 \pm 0.04103$ (top panel); and $\alpha = 2.01627 \pm 0.1755$; $b = -0.8800 \pm 0.0419$ (bottom) Alt text: Schmidt law.

1).

In the same way, we fitted the plot using H40α peakintensity vs. CS peak intensity PVD, as shown in the bottom panel, by a function

$$\log \frac{I_{\rm H40,max}}{({\rm pc\ cm^{-6}})} = b + \alpha\ \log \frac{I_{\rm CS\ peak}}{({\rm Jy\ beam^{-1}})}, \qquad (5)$$

and obtained $\alpha = 2.016 \pm 0.175$ and $b = -0.880 \pm 0.042$. Both the Schmidt indices, α on the sky and PVD, agree well with each other. We conclude that the power law index of the forward Schmidt relation in the CMZ is $\alpha \simeq 2.0$.

Figure 14 is a simultaneous plot of the running mean values presented in figure 5 without error bars. The straight line shows

Table 1. The Schmidt-law index (slope) α fitted to the forward branches of the TT plots of CMZ using continuum intensity and CS (2-1) integrated intensity on the sky and on the LVD using the peak intensities of H40α abd CS (2-1) lines (figure 13)

Method	α	SFR coefficient b
TT on the sky	2.055 ± 0.044	4.613 ± 0.041
TT on the LVD	2.016 ± 0.175	-0.880 ± 0.042

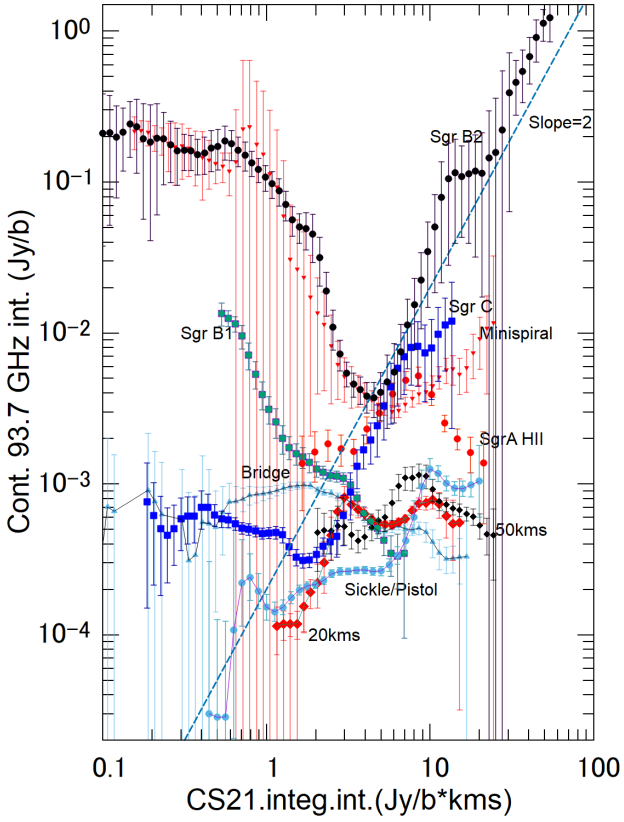


Fig. 14. Overlay of running averaged Schmidt plots by 93.7 GHz continuum to CS21 integ. int. for various regions. Alt text: Schmidt plots for various regions.

a relation with $\alpha = 2$, as obtained for the EM-CS plot and H40α-CS (2-1) plot using PVD. Although the absolute value varies from region to region, the increasing branches corresponding to the forward Schmidt relation are reasonably parallel to the $\alpha = 2$ line.

7.2 Schmidt index 2 indicative of cloud collision trigger of star formation

We have shown that the forward branches of the Schmidt plot in the CMZ, as well as in individual HII regions, have a common index value of $\alpha \simeq 2$. This index (slope) indicates that star formation in the CMZ is predominantly triggered by the collision process between clouds or filaments of molecular gas.

This supports the pioneering finding of the cloud collision process in the Sgr B2 molecular cloud complex by the CO line observations with the Nobeyama 45-m telescope at $\sim 15''(\sim 0.6\ \ {\rm pc}\ )$

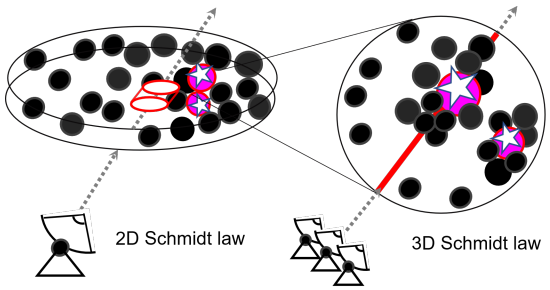


Fig. 15. Resolved 3D Schmidt analysis of the CMZ, which resolves one single point of the current 2D works for galaxies at 100 pc resolution. Alt text: 2D and 3D Schmidt relations.

resolution (Hasegawa et al. 1994). The collision scenario has also been suggested for the 20- and 50-km s^{-1}clouds (Tsuboi et al. 2015; Tsuboi et al. 2021), but the present analysis was not sensitive enough to prove it in these clouds.

The cloud collision scenario is a natural consequence of the highly dynamical and turbulent circumstances in the Galactic Center (Kruijssen et al. 2019; Kruijssen et al. 2019; Dale et al. 2019; Ridley et al. 2017; Sormani et al. 2022; Tress et al. 2020; Hunter et al. 2024). In such circumstances, gravitational instability is suppressed due to strong shear motion. High-velocity differential rotation in the deep gravitational potential of the CND also suppresses the regular instability (Sofue et al. 2026a). Therefore, some external forces, such as collisions, may be required to compress a cloud to form stars.

This is in contrast to the $\alpha = 1$ index generally observed in the disks of the Galaxy and spiral galaxies (Fuchs et al. 2009; Willis et al. 2015; Bacchini et al. 2019; Spilker et al. 2021; Elia et al. 2022; Sofue & Nakanishi 2017; Sofue 2017; Sofue 2024), indicative of stochastic star formation in steady giant molecular clouds due to self-regulating contraction by gravitational instability, where the Jeans time of the cloud is safely shorter than the dynamical timescale of galactic rotation.

7.3 Sub-pc Schmidt relation

One notable finding in the present analysis is that the Schmidt relation holds at a sub-parsec resolution, here at $2''.45 (0.097\ \mathrm{pc})$, which has already resolved the major clouds. This means that the relation arises not only from the two dimensional spatial correlation between the HII regions and clouds projected on the sky but also from the correlation between quantities integrated along the lines of sight, as illustrated in figure 15. This situation is in contrast to the 2D Schmidt relation obtained for the more face-on disk of the spiral galaxy M33, where the law breaks down at scales smaller than the typical size of GMCs, ~ 80 pc (Onodera et al. 2010).

7.4 CS-to-H_2 conversion factor, $X_{\rm CS21}$

In order to represent the Schmidt relation in terms of the SFR and gas column density, we need to convert the observed CS (2-1) intensity into H_2column density. For this, we normalize the CS (2-1) intensity by that of the CO line emission well studied in the current CMZ studies.

The area-integrated CS-line intensity of CMZ on the sky is given by

$$I_{\rm tot} = \int I_{\rm CS} dxdy = 5.22 \times 10^3\ [\mathrm{Jy\ beam^{-1}\ pc^{\ 2}}]. \quad (6)$$

We then assume that this total intensity is proportional to the total molecular mass of $M_{\rm tot} = M_{\rm CMZ} = \gamma_{\rm gas} 10^7 M_\odot$, which is γ times the estimated molecular mass of the CMZ from the CO-to-H_2 conversion factor of $X_{\rm CO} = 0.51 \times 10^{20} \mathrm{H_2\ cm^{-2}[K\ km\ s^{-1}]^{-1}}$ and the mean molecular weight of $\mu = 1.4$ (Sofue 2022). Remembering that 1 Jy beam^{-1}= 26 K in our synthesized beam, we have a conversion relation between H_2column density and CS (2-1) integrated intensity as

$$N_{\rm H_2} = \gamma X_{\rm CS} I_{\rm CS21}, \quad (7)$$

where

$$X_{\rm CS} = 3.3 \times 10^{22}\ \mathrm{H_2\ cm^{-2} (K\ km\ s^{-1})^{-1}}, \quad (8)$$

with γ being a correction factor of the total molecular mass of CMZ in units of $10^7 M_\odot$.

7.5 SFR-$\Sigma_{\rm H_2}$ relation and comparison with current Schmidt relations for galaxies

The SFR is usually determined by the Hα line luminosity (Kennicutt et al. 1994). Since the GC is almost totally opaque to the optical recombination lines, the radio recombination lines (RRL), which are optically thin, are an alternative to Hα.

We use the EM based Schmidt relation given by equation (4) to obtain the surface-SFR to surface-mass expression of the Schmidt relation given by equation 1. First, we express the SFR in terms of the emission measure as

$$\frac{SFR}{(M_\odot\ \mathrm{kpc^{-2}}\ yr^{-1})} \sim \Gamma \times 7.7 \times 10^{-6} \frac{EM}{(\mathrm{pc\ cm^{-6}})} \quad (9)$$

where $\Gamma \sim 0.1$ is a correction factor defined by

$$\Gamma = \gamma_{\rm cool} \gamma_{\rm disk} / \gamma_{\rm OB\ mass} / \gamma_{\rm OB\ Lum} / \gamma_{\rm UV} / \tau_6 \sim 0.1 \quad (10)$$

Here,

$$\gamma_{\rm cool} = \Lambda(T_{\rm e}) / 10^{-23} \mathrm{erg\ cm^{+3}\ s^{-1}} \sim 0.1 \quad (11)$$

is the correction for the cooling coefficient $\Lambda(T_{\rm e})$ at $T_{\rm e} \sim 6000$ K (Sofue et al. 2016; Raymond et al. 1976; Foster et al. 2012);

$$\gamma_{\rm disk} = b_{\rm disk} / a_{\rm disk} \sim 0.1 \quad (12)$$

is the correction for the line of sight depth with $a_{\rm disk}$ and $b_{\rm disk}$ being the radius and half thickness of the disk, respectively, estimated from the latitudinal amplitude of the warped 120-pc molecular ring (Sofue 2022);

$$\gamma_{\rm OB\ mass} = M_{\rm OB} / M_{\rm born\ stars} \sim 0.1 \quad (13)$$

is the ratio of OB to the total mass of newly born stars;

$$\gamma_{\rm OB\ lumi} = L_{\rm OB} / 10^4 L_\odot \sim 10 \quad (14)$$

is the luminosity of the OB star in units of $10^4 L_\odot$; and

$$\gamma_{\rm UV} = L_{\rm HII} / L_{\rm OB} \sim 0.1 \quad (15)$$

is the efficiency of UV photon absorption by the hydrogen gas, with $L_{\rm HII}$ as the cooling rate (luminosity) of the HII region; and

$$\tau_6 = \tau_{\rm OB} / 10^6 \mathrm{y} \sim 1 \quad (16)$$

the lifetime of OB stars in units of 10^6 y.

The surface mass density is calculated by

$$\frac{\Sigma}{M_\odot\ \mathrm{pc^{-2}}} = \gamma_{\rm mol\ mass} \gamma_{\rm disk} \times 1.9 \times 10^3 \frac{I_{\rm CS21integ.int}}{\mathrm{Jy\ beam^{-1}\ km\ s^{-1}}}, \quad (17)$$

where

$$\gamma_{\rm mol\ mass} = M_{\rm tot.mol.mass}/10^7\ M_\odot \sim 1 \qquad (18)$$

is the correction factor for the total molecular gas mass of the CMZ related to intensity by equation 6.

Using these formulations of the SFR and surface mass density of molecular gas, we re-plot the EM-based Schmidt relation in figure 16. The forward branch can be fitted by a relation

$$\frac{SFR}{M_\odot\,{\rm kpc}^{-2}\,{\rm y}^{-1}} \sim 1.0\times10^{-6}\left(\frac{\Sigma}{M_\odot\ {\rm pc}^{-2}}\right)^{2.0}. \qquad (19)$$

as shown by the dashed line in the figure.

7.6 Comparison with the current Schmidt relations

We compare the results with the Schmidt plots for galaxies and starbursts (Kennicutt 1998; Komugi et al. 2006; Komugi et al. 2005). We find that:

- SFR in the forward branch in region (A) of the CMZ is lower than that for starbursts by a factor of 2 to 3, but it approaches the starburst values at the high end due to the steeper slope. This means that Sgr B2 may be regarded as a local starburst site, while the entire CMZ is rather quiet.
- The reverse branch of region (B) for post-SF sites runs distinctly displaced from the Schmidt relation for galaxies toward lower gas density. This branch has been detected for the first time in the present work due to the resolved Schmidt plot.
- Region (C) stands for the background gas of the CMZ, where SFR is lower than that expected from the Schmidt relation of normal galaxies.

8 Discussion

8.1 Uncertainty of SFR-$\Sigma_{\rm H_2}$ diagram

The accuracy of the SFR-$\Sigma_{\rm H_2}$ relation (Schmidt relation) depends directly on the number of correction factors γ_i. Therefore, the relation given by equation (19) is uncertain to an order of magnitude. This situation also applies to any current studies of the KS laws in the literature. Moreover, the present work uses pure radio data from the same telescope and in the same wave band, while other contemporary studies use optical (Hα) and radio (molecular line) observations from different telescopes in a hybrid manner (Kennicutt & Evans 2012). This means that the discussion comparing our results with the current Schmidt relation analysis for galaxies and starbursts is still not conclusive; hence, figure 16 may be considered provisional, and a more precise determination of the coefficients will be necessary for further quantitative discussions.

Below, we provide some possible considerations regarding the interpretation of the ACES SF diagram.

8.2 On-going SF region (A) with forward Schmidt relation

The forward Schmidt branch (A) of the CMZ is almost entirely attributed to the active star formation and dense molecular gas in Sgr B2, as shown in figure 14. This branch (A) aligns slightly below the Schmidt relation for starburst galaxies, as shown in figure 16. Therefore, Sgr B2 is an active star formation region comparable to that of disk-averaged starburst activity. However, this does not mean that the entire CMZ is active; the SF activity is strongly localized to Sgr B2, while the other regions are generally quiet,

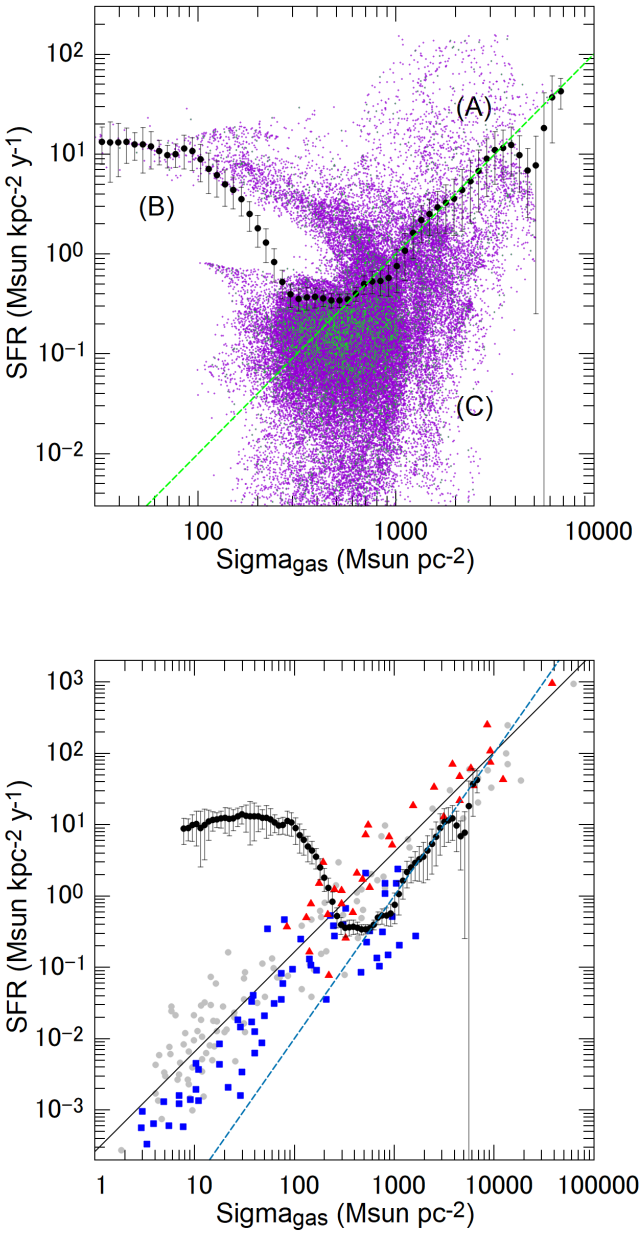


Fig. 16. [Top] The Schmidt relation for the CMZ fitted by region (A) with a slope of $\alpha = 2.0$ by equation 19, compared with [bottom] that for galaxies (grey dots and straight line with a slope of $\alpha = 1.4$) (Kennicutt 1998), and normal galaxies (rectangles) and starburst (triangles), respectively (Komugi et al. 2006; Komugi et al. 2005). The SF activity in CMZ is lower than that in galaxies and starbursts, while the slope is sharper at $\alpha = 2.0$. Alt txt: SFR for galaxies and CMZ.

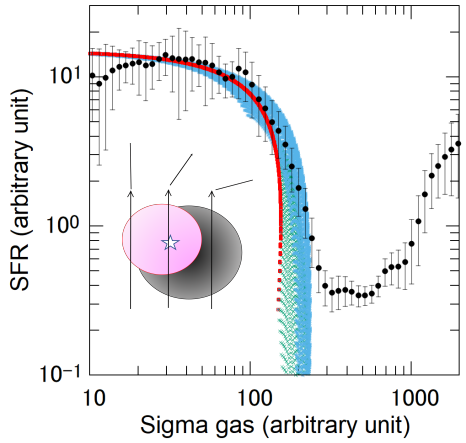


Fig. 17. A simple model for the inverse Schmidt branch for a molecular cloud eroded by an HII region, compared with the observation for the CMZ (in arbitrary axis scalings). Insertion illustrates the lines of sight and corresponding positions of the branch. The red line represents a case for a concentric HII region. Alt txt: Simulation of inverse Schmidt branch.

comparable to or less than those in normal galaxy disks. This is consistent with the currently reported low overall SF activity in the CMZ (Sofue 2022; Henshaw et al. 2023). The steep Schmidt index $\alpha = 2.05 \pm 0.04$ (table 1) supports the cloud-collision mechanism for the trigger of SF (Hasegawa et al. 1994).

8.3 Inverse Schmidt branch

A possible cause of the inverse Schmidt branch found in Sgr B2 North (figures 4 – 6) and Minispiral (figure 5) is the absorption of the background bright HII continuum emission by the CS cloud in front of the continuum source. This branch does not appear in the plot using the transparent HNCO (4-3) line as shown in figure 6. This particular feature appears only when the molecular cloud is located in front of the HII region and the continuum emission is strong enough as well, while the molecular line from the cloud beyond the HII region is not affected. Statistically, half of the CS emission on the same line of sight to the HII region is affected by this effect. This may have caused an artifact shift of the Schmidt branch toward left by a factor of 1/2, whlie the shape of the branch, hence the index α does not vary.

An alternative mechanism to create the inverse branch is the erosion of molecular clouds by expanding HII regions, as schematically modeled in figure 17. In this case the branch appears even in a plot using a transparent line, which is in fact recognized as a faint inverse branch in the continuum-HNCO plot in figure 6. A similar inverse behavior is also expected in the absorption case.

Since the inverse feature appears in relatively small areas in the analyzed regions, we here neglect the effect as a whole to study the forward Schmidt branch. A detailed analysis of backlight-absorption and erosion effect would be an interesting subject not only for Sgr B2 but also in general Schmidt-law studies including those for the Milky Way disk and galaxies, while it is beyond the scope of this paper.

Table 2. Mass fraction of SF molecular gas in CMZ.

Region type	Total integ. int. $_{\rm pc^2 Jy\,beam^{-1} km\,s^{-1}}$	Fraction %	Mass $M_\odot$
(A) On-going SF site	0.994E+02	1.90	1.9E+5
(B) CS shadow	0.246E+02	0.47	4.7E+4
(C) Non SF reservoir	0.510E+04	97.64	9.8E+6
Total	0.522E+04	100.00	1.0E+7†

† Half of the total mass of CMZ from CO-line measurement for a wider area.

8.4 Molecular reservoir (C) with low or zero SFR

As demonstrated in figure 16, the SFR in the basic molecular region (C) of the Schmidt plot is an order of magnitude lower than that in normal galaxies and starbursts. This means that the efficiency of SF in the CMZ is generally lower compared to that in galaxies and starbursts.

The Schmidt plot can be used to estimate the mass fraction of the molecular gas that is currently being used for star formation by calculating the fraction of gas mass in the forward and reverse branches of the Schmidt plot compared with the remaining majority of gas content. We divide the Schmidt plot into three areas, A, B and C as shown in figure 4: Region A is the on-going SF block with $I_{\rm CS} \geq 4$ Jy beam^{-1}km s^{-1}and $I_{\rm cont} \geq 0.003$ Jy beam^{-1}; region B is CS line-absorbed region against background HII continuum emission with $I_{\rm CS} < 4$ Jy beam^{-1}km s^{-1}and $I_{\rm cont} \geq 0.003$ Jy beam^{-1}; and region C is the non-SF block with $I_{\rm cont} < 0.003$ Jy beam^{-1}. We then calculate the integrated intensity

$$J_{\rm CS} = \Sigma I_{\rm CSdxdy} \qquad (20)$$

in each block, where $dx = dy = 0''.5$ $R_0 = 0.02$ pc are the pixel sizes of the used map.

The calculated result is listed in table 2 for the conversion factor obtained in the previous section. It is emphasized that the mass fraction of molecular gas directly related to star formation in the CMZ is extremely low at ~ 2 % of the total molecular gas. Conversely, the basic (as well as pre-SF) molecular gas in region (C) dominates the CMZ with a mass fraction as high as 98%.

8.5 ACES diagram: generalized molecular SF law

The majority of the molecular clouds spend their lifetimes in region (C) as pre-SF clouds. By collision or self-gravitational instability, a small fraction of the clouds is forced to form stars in region (A), creating the forward Schmidt branch. This branch may mimic the main sequence of stellar evolution.

The ACES diagram is applicable to any interstellar region and galaxy, with an arbitrary resolution; here of 0.1 pc. This contrasts with current KS law analysis, which apply to smoothed data ranging from approximately 100 pc to kpc scales. A paradigm shift in Schmidt's law may be necessary, where we can trace the evolutionary trajectory of SF from the fundamental cloud phase (C), which accounts for 98% of the total gas, to the ongoing star-forming stage (A), which accounts for about 2%.

9 Summary

Using the TT plot (intensity-to-intensity map) between two of the maps of 93.7 GHz radio continuum intensity, the hydrogen recombination line intensity at 99 GHz, and emission measure, we show that these three quantities are linearly proportional to each other,

such that the continuum intensity is representative of EM; hence, the star formation rate (SFR).

Based on this relation, we made a TT plot of the continuum intensity against CS (2-1) integrated intensity of the CMZ, which we call the Schmidt plot or the ACES SF diagram. The plots are categorized into three regions: (A) Molecular clouds associated with SF regions having a forward Schmidt relation with a power law index of $\alpha \sim 2$. (B) Inverse branch caused by self and backlight continuum absorption. and (C) Non-SF (basic) clouds without correlation with star formation regions that dominate the CMZ.

We also applied the TT analysis to individual SF regions and found that Sgr B2 contains both type (A) indicating on-going SF and (B) showing a fraction with back-light absorption and/or cloud erosion by HII regions; Sgr B1 is dominated by the inverse branch (B); and Sgr C is controlled by the forward branch (A), showing an on-going SF region, although the intensity of the SFR is mild.

We then constructed an EM-based Schmidt plot and compared it with the Kennicutt-Schmidt relation for normal galaxies and starbursts. We find that the SFR for the forward-branch of the Schmidt plot of the CMZ, mostly attributable to Sgr B2, is on average a factor of two lower than, but comparable at the high end, to that of the starbursts, while the SFR of the entire CMZ is comparable to or lower than that of normal galaxy disks. The overall Schmidt-law index is as steep as $\alpha = 2$, suggesting that the star formation is triggered by cloud collisions.

Acknowledgments

This paper makes use of the following ALMA data: ADS/JAO.ALMA#2021.1.00172.L. ALMA is a partnership of ESO (representing its member states), NSF (USA) and NINS (Japan), together with NRC (Canada), MOST and ASIAA (Taiwan), and KASI (Republic of Korea), in cooperation with the Republic of Chile. The Joint ALMA Observatory is operated by ESO, AUI/NRAO and NAOJ. The data analysis in this paper was performed at the Astronomical Data Center of the National Astronomical Observatories of Japan.
Y.S. and K.K. acknowledge support from JSPS KAKENHI Grant Number JP24H00004 and JP23K20035
C.B. acknowledges funding from NSF under Award Nos. 2108938, 2206510, and CAREER 2145689, as well as from the National Aeronautics and Space Administration through the Astrophysics Data Analysis Program under Award "3-D MC: Mapping Circumnuclear Molecular Clouds from X-ray to Radio," Grant No. 80NSSC22K1125.
A.G. acknowledges support from the NSF under AAG 2206511 and CAREER 2142300.
X.L. acknowledges support from the Strategic Priority Research Program of the Chinese Academy of Sciences (CAS) Grant No. XDB0800300, the National SKA Program of China (2025SKA0140100), the National Natural Science Foundation of China (NSFC) through grant Nos. 12273090 and 12322305, and the National Key R&D Program of China (No. 2022YFA1603101).
D.R-V acknowledges the financial support of DIDULS/ULS, through the project PR2653856.
J.W. gratefully acknowledges funding from the National Science Foundation under Award Nos. 2108938 and 2206510.
C.F. acknowledges funding provided by the Australian Research Council (Discovery Projects DP230102280 and DP250101526), and the Australia-Germany Joint Research Cooperation Scheme (UA-DAAD). Q.D.W. acknowledges support from NASA via grant GO3-24120X.
Part of this research was carried out at the Jet Propulsion Laboratory, California Institute of Technology, under a contract with the National Aeronautics and Space Administration (80NM0018D0004). DCL acknowledges financial support from the National Aeronautics and Space Administration (NASA) Astrophysics Data Analysis Program (ADAP).

Data availability

The interferometer data were taken from the survey data from ALMA cycle 8 Large Program "ALMA Central Molecular Zone Exploration Survey" (ACES, 2021.1.00172.L).

Conflict of interest

The authors declare that there is no conflict of interest.

References

Bacchini, C., Fraternali, F., Iorio, G., et al. 2019, A&A, 622, A64.
Barnes, A. T., Longmore, S. N., Battersby, C., et al. 2017, MNRAS, 469, 2263.
Barnes, A. T., Longmore, S. N., Avison, A., et al. 2019, MNRAS, 486, 1, 283.
Battersby, C., Santa-Maria, M. G., Lipman, D., et al. 2026, arXiv:2602.20262.
Boissier, S., Prantzos, N., Boselli, A., et al. 2003, MNRAS, 346, 1215.
Burkhart, B. 2018, ApJ, 863, 118
Calzetti, D., Lapeer, D., Kennicutt, R. C., et al. 2026, ApJ, 1008, 2, 198.
Dale, J. E., Kruijssen, J. M. D., & Longmore, S. N. 2019, MNRAS, 486, 3, 3307.
Elia, D., Molinari, S., Schisano, E., et al. 2022, ApJ, 941, 162.
Elmegreen, B. G. & Lada, C. J. 1977, ApJ, 214, 725.
Elmegreen, B. G., & Scalo, J. 2004, ARA&A, 42, 211
Federrath, C. 2013, MNRAS, 436, 1245
Federrath, C., Rathborne, J. M., Longmore, S. N., et al. 2016, ApJ, 832, 2, 143
Foster, A. R., Ji, L., Smith, R. K., et al. 2012, ApJ, 756, 2, 128.
Fuchs, B., Jahreiss, H., & Flynn, C. 2009, AJ, 137, 266.
Fukui, Y., Habe, A., Inoue, T., et al. 2021, PASJ, 73, S1.
Ginsburg, A., et al. submitted to MNRAS.
Gravity Collaboration, Abuter, R., Amorim, A., et al. 2019, A&A, 625, L10.
Habe, A. & Ohta, K. 1992, PASJ, 44, 203
Hacar, A., Clark, S. E., Heitsch, F., et al. 2023, Protostars and Planets VII, 534, 153.
Hasegawa, T., Sato, F., Whiteoak, J. B., et al. 1994, ApJL, 429, L77.
Evans, N. J., Heiderman, A., & Vutisalchavakul, N. 2014, ApJ, 782, 2, 114.
Henshaw, J. D., Barnes, A. T., Battersby, C., et al. 2023, Protostars and Planets VII, 534, 83.
Heyer, M. H., Corbelli, E., Schneider, S. E., et al. 2004, ApJ, 602, 2, 723.
Heywood, I., Rammala, I., Camilo, F., et al. 2022, ApJ, 925, 165.
Hsieh, P.-Y., Walker, D. L., Ginsburg, A., et al. 2026, arXiv:2603.00863.
Hunter, G. H., Sormani, M. C., Beckmann, J. P., et al. 2024, A&A, 692, A216.
Jackson, J. M., Armstrong, J. T., & Barrett, A. H. 1984, ApJ, 280, 608. doi:10.1086/162033
Kennicutt, R. C., Tamblyn, P., & Congdon, C. E. 1994, ApJ, 435, 22.
Kennicutt, R. C. & Evans, N. J. 2012, ARA&A, 50, 531.
Kennicutt, R. C. & De Los Reyes, M. A. C. 2021, ApJ, 908, 1, 61.
Kennicutt, R. C. 1998, ApJ, 498, 2, 541.
Kennicutt, R. C. & Evans, N. J. 2012, ARA&A, 50, 531.
Kennicutt, R. C. & De Los Reyes, M. A. C. 2021, ApJ, 908, 61.
Kimura, T. & Tosa, M. 1996, A&A, 308, 979.
Komugi, S., Sofue, Y., & Egusa, F. 2006, PASJ, 58, 793.
Komugi, S., Sofue, Y., Nakanishi, H., et al. 2005, PASJ, 57, 733.
Kruijssen, J. M. D., Schruba, A., Chevance, M., et al. 2019, Nature, 569, 7757, 519.
Kruijssen, J. M. D., Dale, J. E., Longmore, S. N., et al. 2019, MNRAS, 484, 4, 5734.
Krumholz, M. R., Dekel, A., & McKee, C. F. 2012, ApJ, 745, 1, 69.
Krumholz, M. R., Dekel, A., & McKee, C. F. 2012, ApJ, 745, 69
Longmore, S. N., Bally, J., Barnes, A. T., et al. 2026, arXiv:2602.20340.
Lada, C. J. & Lada, E. A. 2003, ARA&A, 41, 57.
Lu, X., Walker, D. L., Ginsburg, A., et al. 2026, arXiv:2602.20445.
Mac Low, M.-M., & Klessen, R. S. 2004, Rev. Mod. Phys., 76, 125
Morris, M. 1993, ApJ, 408, 496.
Myers, P. C. 2009, ApJ, 700, 1609.
Nonhebel, M., Barnes, A. T., Immer, K., et al. 2024, A&A, 691, A70.
Onodera, S., Kuno, N., Tosaki, T., et al. 2010, ApJL, 722, 2, L127.
Pineda, J. E., Arzoumanian, D., Andre, P., et al. 2023, Protostars and Planets VII, 534, 233.
Raymond, J. C., Cox, D. P., & Smith, B. W. 1976, ApJ, 204, 290.
Ridley, M. G. L., Sormani, M. C., Tress, R. G., et al. 2017, MNRAS, 469, 2, 2251.
Salim, D. M., Federrath, C., & Kewley, L. J. 2015, ApJL, 806, 2, L36.
Schmidt, M. 1959, ApJ, 129, 243.

Line-to-line scatter (TT) plot matrix (The number n in each cell corresponds to "n.png" in the appendix)

		x-axis (map1.fits)													
		H40alpha	HCOplus	H13COplus	NSplus	CH3CHO	CS21	H13CN	HC15N	HC3N	HN13C	HNCO	SO21	SO32	SiO21
y-axis (map2.fits)	H40alpha	–	1	2	3	4	5	6	7	8	9	10	11	12	13
	HCOplus		–	14	15	16	17	18	19	20	21	22	23	24	25
	H13COplus			–	26	27	28	29	30	31	32	33	34	35	36
	NSplus				–	37	38	39	40	41	42	43	44	45	46
	CH3CHO					–	47	48	49	50	51	52	53	54	55
	CS21						–	56	57	58	59	60	61	62	63
	H13CN							–	64	65	66	67	68	69	70
	HC15N								–	71	72	73	74	75	76
	HC3N									–	77	78	79	80	81
	HN13C										–	82	83	84	85
	HNCO											–	86	87	88
	SO21												–	89	90
	SO32													–	91
	SiO21														–

Fig. 18. Matrix of TT plots between various molecular lines Alt txt: TT plots for various molecular lines.

Shu, F. H., Adams, F. C., & Lizano, S. 1987, ARA&A, 25, 23.
Sofue, Y. 2017, MNRAS, 469, 2, 1647.
Sofue, Y. 2022, MNRAS, 516, 1, 907.
Sofue, Y. 2024, PASJ, 76, 3, L15.
Sofue, Y., Habe, A., Kataoka, J., et al. 2016, MNRAS, 459, 1, 108.
Sofue, Y., Oka, T., Longmore, S. N., et al. 2025a, PASJ, 77, 4, 687.
Sofue, Y., Oka, T., Longmore, S. N., et al. 2025b, PASJ, 77, 4, L55.
Sofue, Y., Longmore, S. N., Walker, D., et al. 2026a, PASJ, 78, 2, 536.
Sofue, Y., Longmore, S. N., Walker, D., et al. 2026b, PASJ, in press, arXiv:2608.10227.
Sofue, Y. & Nakanishi, H. 2017, PASJ, 69, 2, 19.
Spilker, A., Kainulainen, J., & Orkisz, J. 2021, A&A, 653, A63.
Sormani, M. C., Gerhard, O., Portail, M., et al. 2022, MNRAS, 514, 1, L1. 5024.
Stone, N., Sari, R., & Loeb, A. 2013, MNRAS, 435, 3, 1809.
Tress, R. G., Sormani, M. C., Glover, S. C. O., et al. 2020, MNRAS, 499, 3, 4455.
Tsuboi, M., Kitamura, Y., Uehara, K., et al. 2021, PASJ, 73, S91.
Tsuboi, M., Miyazaki, A., & Uehara, K. 2015, PASJ, 67, 6, 109.
Uyanıker, B., Reich, W., Yar, A., et al. 2004, A&A, 426, 909.
Willis, S., Guzman, A., Marengo, M., et al. 2015, ApJ, 809, 1, 87.
Walker, D. L., Ginsburg, A., Barnes, A. T., et al. 2026, arXiv:2602.20276.
Paré, D. M., Feng, Z.-X., Hu, Y., et al. 2026, ApJ, 1000, 1, 37.

Appendix 1 Scatter (TT) plots of various pairs of molecular lines

We present TT (scatter) plots for CMZ between various molecular lines that may potentially be useful for further studies of interstellar physics and chemistry in the CMZ. Figure 18 shows the combination of the lines in the used data set. Figure 19 shows the individual plots corresponding to figure 18, but only for viewing on a computer monitor screen using the zoom tool.

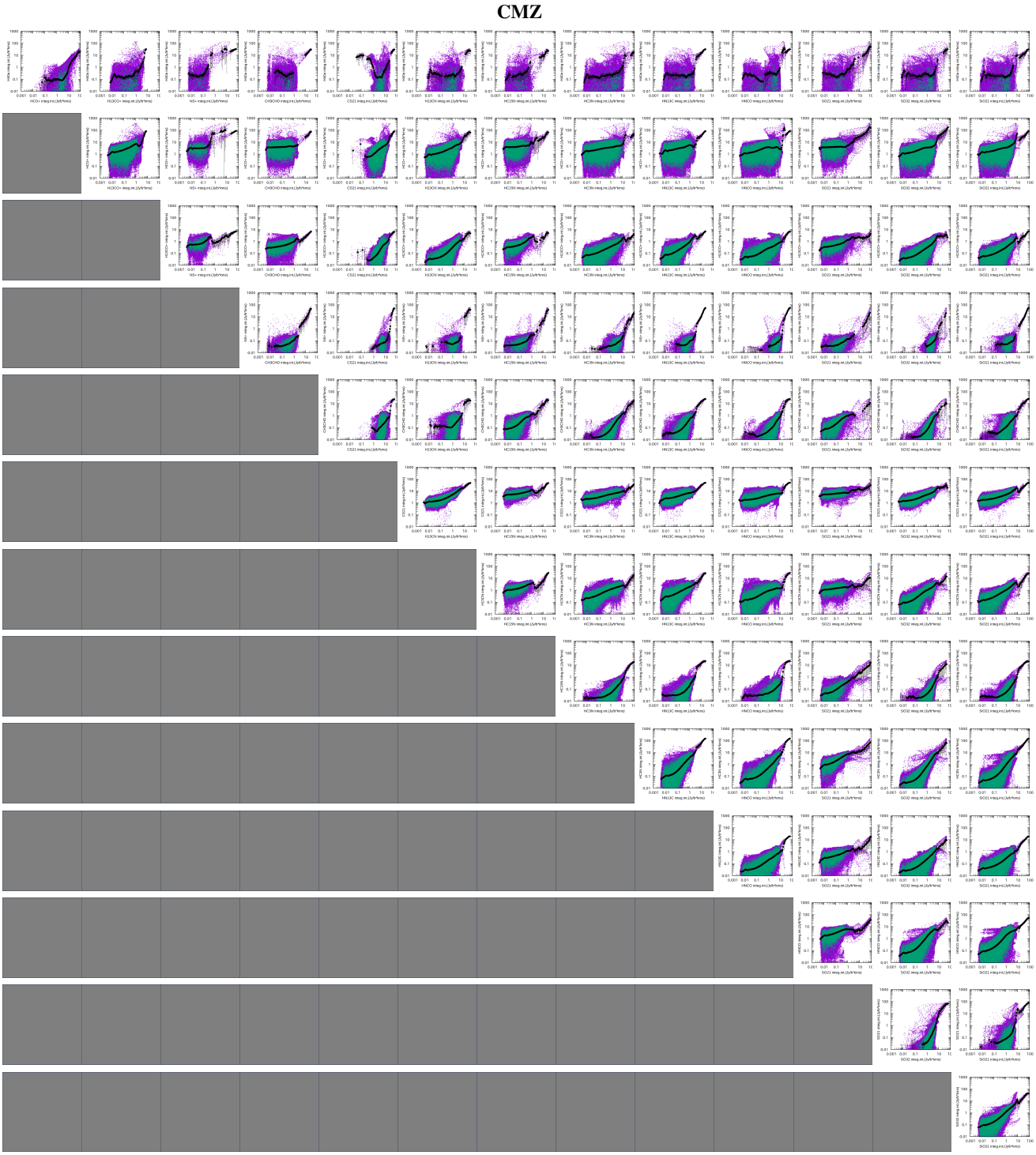


Fig. 19. TT matrix for various molecular lines in the CMZ. Alt txt: TT plots for various molecular lines.